PHYSICAL REVIEW FLUIDS **6**, 033701 (2021)

Suppression of electroconvective and morphological instabilities by an imposed cross flow of the electrolyte

Gaojin Li,[1] Alex Townsend,[2] Lynden A. Archer,[1] and Donald L. Koch[1,*]

[1]*Robert Frederick Smith School of Chemical and Biomolecular Engineering, Cornell University, Ithaca, New York 14853, USA*

[2]*Department of Mathematics, Cornell University, Ithaca, New York 14853, USA*

(Received 13 June 2020; accepted 26 February 2021; published 10 March 2021)

Electroconvective (EC) instability and its influence on surface morphological perturbations (Morph) are important in many applications, including electrodialysis, batteries, and fuel cells. In this work, we study the effects of a two-dimensional channel flow on the EC and Morph instabilities using two approaches. In the bulk analysis, we derive the asymptotic solutions for small and large wave numbers by neglecting the space charge layer and imposing a second kind electroosmosis slip velocity boundary condition on the electroneutral bulk region. In the full analysis, the instability of the entire region of the liquid electrolyte is analyzed using the ultraspherical spectral method. Both studies show that the flow significantly affects the EC instability. The imposed flow distorts the concentration field, causing a sheltering effect which hinders the ion transport from low- to high-concentration regions, and therefore suppresses the EC instability below a certain wave number. In combination with the viscous stabilization of the high wave number modes by the space charge layer, a sufficiently strong imposed flow can fully suppress the EC instability. The increment in the critical voltage for the instability onset is roughly proportional to the square root of the product of imposed velocity and double layer thickness. The imposed flow has a smaller effect on the Morph instability, except that it may remove the morphological modes resulting from the EC instability and thereby change the wave number of the most unstable mode.

DOI: 10.1103/PhysRevFluids.6.033701

I. INTRODUCTION

The interaction between an imposed flow and the electroconvection of a liquid electrolyte is important in many applications: desalination [1], rotating disk electrodeposition, and fuel cells [2]. Experiments and simulations show that an imposed channel flow modifies the patterns of EC vortices near a fixed ion-selective surface [3] and significantly increases the ion flux [4]. On a metal electrode surface, the imposed flow affects the morphology of the electrodeposition by inducing Taylor vortex streets along streamlines [5]. More recently, linear stability analyses by Parekh and coworkers showed that the forced advection of ions by normal [6] and tangential [7] imposed velocities has a stabilizing effect on the morphological (Morph) instability. However, these studies neglected the perturbation of the velocity field induced by morphological perturbations [6] as well as electroconvective flows. The present study provides a theoretical understanding of the influence of the imposed flow on the EC instability in the presence (EC/Morph) and absence (EC) of morphological evolution of the interface.

---

[*] dlk15@cornell.edu

In the absence of the imposed flow, purely electroconvective (EC) instability near a fixed ion-selective surface [8,9] and inlets of the nanofluidic channels connecting two micro-chambers of ion solutions [10,11] has been widely studied in the literature using theories [12–15], experiments [8,9], and direct numerical simulations [16–20]. More discussion on fundamental physics and applications of EC instability can be found in reviews [21,22]. Near a surface such as a Nafion membrane, the ions simply pass through the membrane without changing the morphology of the surface. At a small voltage, the current is sustained by a one-dimensional ion transport by migration and diffusion, and the electrolyte remains quasielectroneutral except that it forms a nanometer-sized nonelectroneutral electric double layer near to the membrane. With increasing voltage, the strong depletion of the ions near the membrane forms a nonequlibrium double layer, which has a micrometer-sized extended space charge layer outside the original equilibrium double layer. Inside the space charge layer, the perturbation of the electric force and the osmotic pressure generate an electroosmosis slip velocity. The osmotic slip velocity, which is called second kind to differentiate from the slip velocity caused by the equilibrium double layer, is the fundamental cause of electroconvection. Rubinstein and coworkers have conducted a series of works to investigate this type of instability using two types of analyses, the bulk analysis and the full analysis. In the first approach, the linear stability analysis is performed only in the electroneutral bulk region, and the contribution of the space charge layer is represented by the slip velocity, which is determined by the properties of the bulk region [12,13]. This simplification facilitates an analytical treatment and predicts the existence of a critical voltage for the onset of the instability. However, it is only qualitatively correct and its prediction of the critical voltage is substantially lower than the one observed in direct numerical simulations [16,18]. In the full analysis [15], the entire electrolyte, including the bulk region and the thin layers near the membrane, is considered by solving the anion and cation conservation equations separately. In this analysis, both the one-dimensional base state solution and the eigenvalue problem for the perturbed equation are numerically solved. The prediction of the critical voltage for the onset of EC instability based on the full analysis quantitatively agrees with the direct numerical simulations [16]. The full analysis also predicts a stable mode at sufficiently high wave number in contrast to the bulk analysis, which has the "short-wave catastrophe" [15]. The numerical calculation in the full analysis is challenging because the double layer is much thinner than the bulk region (typically by four to seven orders of magnitude). Typical spectral methods easily become ill conditioned since they require a large number of grid points to resolve the thin layer. In this work, we will use both methods to build a complete understanding of the EC and EC/Morph instabilities.

On a metal electrode surface, the electrodeposition of the metal ions from their salt solutions causes the Morph instability and generates ramified structures. This instability is common in solidification processes and is caused by the "Mullins-Sekerka"-type unstable phase transformation from liquid into solid [23]. Although this morphological instability does not require electroconvective flow, the EC instability, when present, modulates the morphological evolution of the electrodepositing surface [24,25]. Depending on the type of salt, the ion concentration, and the applied field, the deposition can have different morphologies, such as fractal, dense branching, and needle-like [26–28]. Chazalviel found that the fast ramified growth is directly related to the formation of a space charge layer [29]. In his study, the deposit is modeled as a comb of rectilinear equally spaced needles of infinitely small thickness. In a steady solution without a flow, the advancing speed of the deposits equals the retreating speed of anions in the applied electric field near the electrode surface. In the presence of fluid flow, the net charges at the tips of the deposits induce vortices, which bring more ions to the tips and further amplify the needle growth [30]. This positive feedback between electroconvection and the Morph instability is directly observed in experiments [24,25]. The uncontrolled electroconvection near deposition can also lead to different morphologies under similar depositing conditions and generate depositions of network structures [31]. In applications related to batteries and energy storage, many efforts have been devoted in order to suppress the EC and Morph instabilities and achieve stable deposition. Such examples include coating a thin layer of a cross-linked polymers on the electrode surface [32–35], adding agar gel to modify the deposition morphology [36,37], adding high-molecular-weight polymers into the liquid electrolyte [38,39], and adding the polymer-grafted colloids [40]. Our previous study shows that the electroconvection can be stabilized by adding polymers to exert extra drag to the liquid electrolyte [41]. Other studies show that the electroconvection can be suppressed by increasing the resistance to flow with a buoyancy force [42] or boundary confinement [43]. Generally speaking, these results are consistent with the analysis for a Newtonian electrolyte which predicts that the critical voltage for the onset of electroconvection increases with increasing fluid viscosity [12].

The mechanism by which the imposed flow modulates the EC and Morph instabilities is very different from the mechanisms by which rheological modifications alter these instabilities. The imposed flow advects the concentration field and affects the instabilities by altering the base state and/or by directly modifying the perturbation modes. Most previous studies have focused on the first effect. For example, on a rotating disk, the flow brings more ions to the electrode and creates a concentration boundary layer whose thickness is inversely proportional to the square root of the rotation rate [44]. The increased ion concentration near the electrode helps smooth the electrodeposition at microscales [45] and creates spiral deposition structures of millimeter width following the streamlines [46,47]. In a developing boundary layer within a microchannel, the velocity enhances the ion flux perpendicular to the flow direction [4] and interacts with the EC vortices near the boundary layer. Kwak *et al.* showed that the pressure-driven flow reduces the height of the EC vortices as $d \sim V^{2/3}/U_m^{1/3}$, where V is the voltage and U_m is the maximum velocity of the imposing flow [3]. At a high flow rate, the strong mainstream flow confines the fluctuations of electroconvection in the near-wall region and can even fully suppress the EC instability. At low flow rate or/and high voltage, large vortices are swept downstream by the imposed flow [4]. Because of the small thickness of the channel in the direction perpendicular to the flow-electric-field plane, the flow and concentration fields in these examples are nearly two dimensional. In comparison, a flow in a wide channel induces helical vortices originating from the side walls and generates a nonmonotonical overlimiting current dependence on the channel width [48]. Two-dimensional numerical simulations of electroconvection in a electrodialysis cell were numerically studied in Refs. [49,50]. These simulations are performed at a relatively low flow rate and no full suppression of EC flow has been observed. The vortices increase the current and their unsteady motion generates strong oscillations in current. More discussion on flow-through electrodialysis membrane cells in the overlimiting current regime can be found in a recent review paper [51]. However, it is still unclear whether the imposed flow can stabilize the EC flow without altering the concentration field in the base state.

In a channel flow with a fully developed boundary layer, the base state ion concentration is the same as the one-dimensional (1D) steady profile in the absence of the flow. This occurs for a channel whose length is much larger than the entrance region, i.e., $L_x/L_z \gg \mathrm{Pe}_U^{1/3}$, where Pe_U is the Peclet number based on the imposed velocity. As we will see later, however, our analysis also agrees reasonable well with simulations of a developing boundary layer [3]. The theory is applicable to numerical simulations with periodic boundary conditions in the flow direction and experiments with a recycled electrolyte. With this simplification, we study the linear stability of a channel flow of electrolyte in the limiting current regime and provide quantitative prediction of the critical velocity of the imposed flow needed to fully suppress electroconvection and its morphological consequences.

EC instability of a fully developed channel flow can also be observed at the interface between two fluids of different conductivities in a strong electric field [52–54]. In these studies, the applied electric field acts parallel to the flow, and the diffusive mixing layer between the two fluids plays the role of a space charge layer. At higher voltages, the flow exhibits a sequence of transitions from steady to time periodic and then to aperiodic, chaotic states [54], similar to the flows near an ion-selective membrane [49,50]. Stability analysis shows that the onset of the convective instability occurs when the electroviscous velocity is strong enough to compete with diffusion and disturb the mixing layer [52,53]. As we will see later, this mechanism is different from the flow near an ion-selective membrane, where the instability can be suppressed by a strong imposed flow. Interactions between the electrohydrodynamic instability and the imposed flow at high Reynolds numbers were also studied for their applications in electrostatic precipitators for particulate emission reduction and bioaerosol sampling, electrohydrodynamic pumps and mixers, flow control by injecting ions, and heat transfer enhancement [55]. Zhang and coworkers studied the instabilities of a Poiseuille flow of nonconducting dielectric fluid with a unipolar ion injection at a high Reynolds number [56–58]. In their studies, the ions are directly injected near one of the channel walls to create a layer of large charge density. Their results showed that increasing the strength of the electric field changes the modes of the unstable waves [58]. The instability of the flow is complicated due to the coexistence of two types of instability mechanisms, electrohydrodynamic and inertial mechanisms.

In this work, we consider the interaction between the electrohydrodynamic instability and an imposed flow which is perpendicular to the applied electric field. The fluid inertia is negligible and the only mechanism of instability is electrohydrodynamic caused by the formation of the space charge layer. Compared to previous studies, a distinct feature of this work is that the double layer and space charge layer near the ion-selective surface are extremely thin compared to the channel width. For example, in a typical aqueous electrolyte of concentration 1–10^3 mol/m^3, the thickness of the double layer is around 0.1–1 nm, the space charge layer is around 1 μm, and the channel width is typically around 1 mm. The smallest and largest length scales differ by six orders of magnitude. As mentioned before, the bulk analysis uses a slip velocity to replace the thin layers, but its results are only qualitatively correct at small wave numbers. In the full analysis, the widely adopted Chebyshev collocation spectral method is numerically unstable because the discretized eigenvalue problem becomes highly ill conditioned with more than 100 collocation points. To resolve this issue, we use the ultraspherical spectral method [59] to solve both the base and perturbed equations in the full analysis. A detailed comparison between the two approaches are made for both the EC and EC/Morph stability problems.

In most experiments, the EC instability mainly occurs in the flow-electric field plane because the confinement in the third direction restricts the out-of-plane wave vectors from occurring. Therefore, we only consider the two-dimensional flow instabilities in the flow-electric field plane. To simplify the problem, we neglect the entrance region and only consider the modal instability of the fully developed flow. This simplification is valid when the ion concentration polarization along the flow occurs rapidly under a relative strong electric field. Two problems will be considered, the purely EC instability with planar surface and the EC/Morph instability in the presence of an evolving electrode surface. For the EC problem, our goal is to understand the influence of the imposed flow on the modes at different wave numbers and find the critical conditions to partially or fully suppress the EC modes. The mechanism by which the imposed flow suppresses the EC instability is investigated. For the EC/Morph problem, we will see that the imposed flow attenuates the morphological signal of the electroconvective instability while leaving the Mullins-Sekerka instability modes nearly unaltered. For both problems, the analysis is compared with experimental and simulation results from the literature. In the following, we describe the problem setup and the governing equations in Sec. II. In Sec. III, we conduct the bulk analysis and use the resulting analytical solution to gain a physical understanding of the instability. Then, we will consider the full problem by numerically solving the eigenvalue problems in Sec. IV. The physical mechanisms by which the imposed flow alters the instabilities will be discussed. A detailed comparison between the two analyses will be performed to evaluate the viability of the bulk analysis. Summary and conclusions are presented in Sec. V.

II. PROBLEM SETUP AND GOVERNING EQUATIONS

As shown in Fig. 1, we consider a pressure-driven flow of a binary univalent electrolyte in a channel of width $2L$. The applied voltage V is perpendicular to the flow direction and buoyancy effects are neglected. The channel walls only allow a nonzero cation flux, and we will consider two types of surfaces, ion-selective membranes which allow only an EC instability and metal electrode surfaces with interacting EC and Morph instabilities. We only consider the Morph instability of the anode surface where ions are deposited, since experiments show that the stripping process on the cathode surface is typically uniform. Figure 2 shows the distribution of ion concentration and

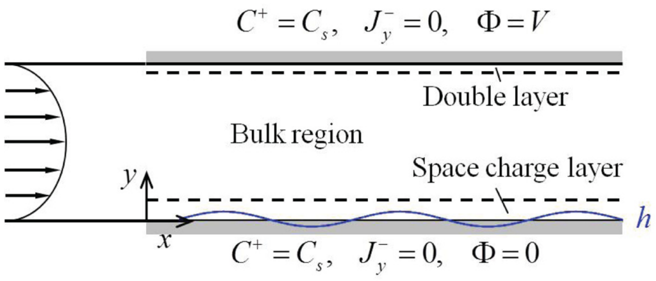

FIG. 1. Schematic of a fully developed cross flow of an electrolyte between two ion-selective surfaces.

potential for fully developed ion transport. The base state is assumed to be quasisteady because the perturbation typically grows much more quickly than the variation of the concentration field. In the base state, the electrolyte inside the channel has three regions at the limiting current: the quasielectroneutral bulk region with a linear ion concentration profile, the equilibrium double layer at the top surface, and the nonequilibrium double layer which has an extended space charge layer at the bottom surface. We neglect the entrance region of the flow and consider the temporal instability of the fully developed region with a uniform space charge layer.

Following the precedent of previous studies [12,15,16,18], we neglect complications such as nonideal solution effects and preferred orientation of ion deposition and apply the equations for ideal ion transport to capture the basic physical trends. The governing equations of the problem include the Nernst-Planck equations for the conservation of ion concentration, the Poisson equation for the electrical potential, and the Stokes equation for the incompressible fluid. In nondimensional form, the equations are

$$\frac{\partial C^+}{\partial t} + \mathrm{Pe}(\boldsymbol{u}\cdot\nabla)C^+ = \frac{1+D}{2}\nabla\cdot(\nabla C^+ + C^+\nabla\Phi), \tag{1a}$$

$$\frac{\partial C^-}{\partial t} + \mathrm{Pe}(\boldsymbol{u}\cdot\nabla)C^- = \frac{1+D}{2D}\nabla\cdot(\nabla C^- - C^-\nabla\Phi), \tag{1b}$$

$$-2\delta^2\nabla^2\Phi = C^+ - C^-, \tag{1c}$$

$$-\nabla p + \nabla^2\boldsymbol{u} + (\nabla^2\Phi)\nabla\Phi = 0, \quad \nabla\cdot\boldsymbol{u} = 0, \tag{1d}$$

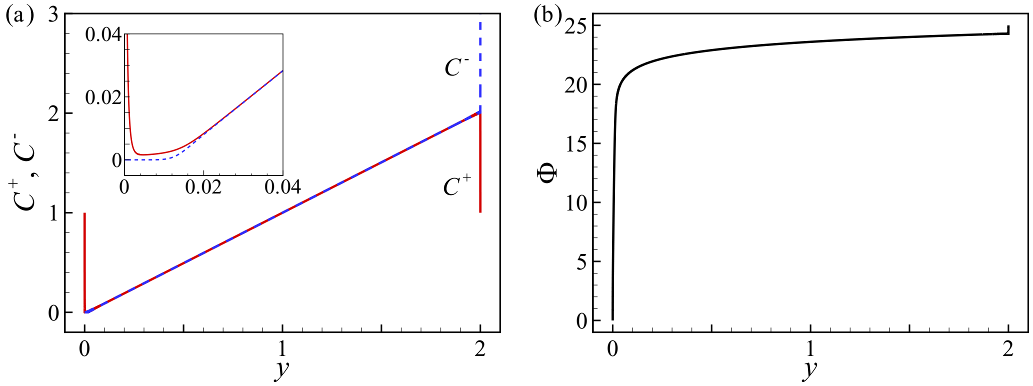

FIG. 2. Distributions of (a) ion concentration and (b) potential of the full base state solution at $V = 25$, which has a nonequilibrium double layer with a space charge layer at $y = 0$, an equilibrium double layer at $y = 2$, and a quasielectroneutral bulk region in between. The bulk analysis only considers the bulk region. The normalized double layer thickness is $\delta = 10^{-4}$ and the current is $I = 2.0241$.

where C^+ and C^- are cation and anion concentrations, Φ is potential, p is pressure, and $\boldsymbol{u}$ is fluid velocity. $D = D^+/D^-$ is the ratio of the cation and anion diffusivities, $\delta = \sqrt{\varepsilon\varepsilon_0 RT/2F^2C_0}/L$ is the dimensionless double layer thickness, L is the half interelectrode distance, ε is the dielectric constant, ε_0 is the vacuum permittivity, R is the ideal gas constant, T is temperature, F is Faraday's constant, and C_0 is the average ion concentration. $\mathrm{Pe} = U_0L/D_0$ is the Peclet number, $U_0 = \varepsilon\varepsilon_0(RT/F)^2/\eta L$ is a characteristic velocity derived by balancing the characteristic Maxwell stress $\varepsilon\varepsilon_0(RT/F)^2$ and the viscous stress $\eta U_0/L$, η is the fluid viscosity, and $D_0 = 2D^+D^-/(D^+ + D^-)$ is the average ion diffusivity. Following Ref. [14], lengths are nondimensionalized by L, velocity by U_0, time by L^2/D_0, ion concentration by C_0, potential by RT/F, and stress by $\eta U_0/L$.

We now discuss the boundary conditions at the two surfaces. On a nonfixed ion-selective surface, such as metal electrodes, the ion deposition and stripping continuously change the average heights of the surfaces. We choose a reference frame moving with the same velocity as the cathode surface which has uniform stripping. In this frame, the deformation of the anode surface is perturbed around $y = 0$, and the cathode surface is fixed at $y = 2$. The growth of the anode surface is represented by $y = h(x, t)$. At the two surfaces, the conditions for ion concentration, potential, and fluid velocity are

$$C^+|_{y=h} = C_s, \quad C^+|_{y=2} = C_s', \quad \boldsymbol{n}\cdot(\nabla C^- - C^-\nabla\Phi)|_{y=h,2} = 0, \tag{2a}$$

$$\Phi|_{y=h} = 0, \qquad \Phi|_{y=2} = V, \tag{2b}$$

$$\boldsymbol{n}\cdot\boldsymbol{u}|_{y=h} = \frac{1}{\mathrm{Pe}}\frac{\partial h}{\partial t}\frac{1}{|\boldsymbol{n}\cdot\boldsymbol{e}_y|}, \quad \boldsymbol{n}\cdot\boldsymbol{u}|_{y=2} = 0, \quad (\mathbf{I} - \boldsymbol{n}\boldsymbol{n})\cdot\boldsymbol{u}|_{y=h,2} = 0, \tag{2c}$$

$$\frac{1+D}{2}\left(\frac{\partial C^+}{\partial y} + C^+\frac{\partial\Phi}{\partial y}\right)\bigg|_{y=h} - I = \frac{1}{v_m}\frac{\partial h}{\partial t}\frac{1}{|\boldsymbol{n}\cdot\boldsymbol{e}_y|}. \tag{2d}$$

In Eq. (2a), we assume the electrochemical potential of the cation is at equilibrium on the electrode surfaces and therefore the cation concentration is fixed. Its specific value does not qualitatively change the results and $C_s = C_s' = 1$ is used in this study. This equilibrium condition is valid when the rate coefficient for ions passing through or depositing on the surface is much larger than the ion transport rate coefficient. The surfaces are impermeable to anions. $\boldsymbol{n}$ is the unit normal vector of the anode surface pointing into the electrolyte. Equation (2b) is the condition for the applied potential. For the ion-selective membrane, this condition is valid in the fully developed regime when the current reaches a constant. In Eq. (2c), $\boldsymbol{e}_y$ is the unit y vector, and $\mathbf{I}$ is the identity matrix. The first equation indicates that the growth of the anode generates a normal velocity of the electrolyte, while the other equations are the usual no-slip and no-penetration conditions of the fluid. Equation (2d) indicates that the growth rate of the perturbed anode surface is determined by the local cation flux minus the constant base state current I. Here, $v_m = v_m^* C_0$ is the dimensionless molar volume of the metal and v_m^* is the dimensional molar volume. The volume change of the solution during charge and discharge is neglected. For ion-selective membranes without a Morph instability, $h \equiv 0$ and Eq. (2d) becomes a trivial condition.

The governing equations (1) with boundary conditions (2) are first solved for the base state. In the base state, $h = 0$, and the pressure-driven flow, ion concentrations, and electric field change only along the y direction, so that the equations become

$$\frac{1+D}{2}\left(\frac{\partial C^+}{\partial y} + C^+\frac{\partial\Phi}{\partial y}\right) = I, \quad \frac{\partial C^-}{\partial y} - C^-\frac{\partial\Phi}{\partial y} = 0, \tag{3a}$$

$$-2\delta^2\frac{\partial^2\Phi}{\partial y^2} = C^+ - C^-, \tag{3b}$$

with boundary conditions

$$C^+|_{y=0} = C_s, \quad \int_0^2 C^- dy = 2, \tag{4a}$$

$$\Phi|_{y=0} = 0, \quad \Phi|_{y=2} = V. \tag{4b}$$

The fluid exhibits Poiseuille flow with $u = U_m y(2-y)$ and $v = 0$, where U_m is the maximum fluid velocity. Eqution (3a) states that in the base state the current I is driven by the cation flux and the anion flux vanishes at any cross-section plane in the electrolyte. In Eq. (4), the condition for the anion means that its total concentration is conserved inside the channel due the no flux conditions on both surfaces. The full base state governed by Eq. (3) requires a numerical solution. Figure 2 shows the full base state solutions for ion concentration and potential at steady state at the limiting current. Here, $\delta = 10^{-4}$ and $V = 25$. The full base state solution has three parts: a nonequilibrium double layer which includes a space charge layer at $y = 0$, an equilibrium double layer at $y = 2$, and a quasielectroneutral bulk region. The imposed velocity has no influence on the base state ion flux in the fully developed channel flow, while it interacts with the linear stability perturbations and affects the EC/Morph instability. The base state solution of the bulk region will be discussed in Sec. III.

The bulk analysis deals with the approximate solution of Eq. (3) by taking advantage of the condition $\delta \ll 1$. In a typical electrochemical system, the normalized double layer thickness is $10^{-7} < \delta < 10^{-3}$, and the difference between cation and anion concentrations is of order δ^2 in the bulk region. The space charge layer thickness $\delta_s \sim (\delta V)^{2/3}$ is also small as long as the overpotential $V \ll |\ln \delta|$ [14]. In the bulk analysis, the effects of these thin layers are replaced by electroosmotic slip velocities [12–14]. To establish a physical understanding of the effects of the imposed cross flow on the linear instability, we will first discuss the bulk analysis in Sec. III. The full analysis will later be considered in Sec. IV.

In typical experiments with aqueous electrolytes, the half interelectrode distance is around 1 mm, the double layer thickness ranges from 0.1 to 1 nm, the dynamic viscosity $\eta = 10^{-3}$ Pa s, the dielectric constant of water $\varepsilon = 80$, ion concentration $C_0 = 0.01$–1 M, the ion diffusivity 10^{-9} m^2/s, the ion transference number $t_c = D^+/(D^+ + D^-) = 0.4$, the molar volume of the metal atom $v_m^* = 1.3 \times 10^{-5}$ m^3/mol. Here, we have cited parameters for lithium ions, but the specific values do not affect the qualitative results in this study. The applied voltage is 1–5 V, and the typical velocity in a microchannel is up to 10^4 μm/s. Based on these parameters, we choose $\mathrm{Pe} = 0.35, \quad D = 0.67, \quad v_m = 0.013, \quad U_m = 0 \sim 10^4$, and $\delta = 10^{-5}$–10^{-3} for this study.

III. BULK ANALYSIS

In the bulk region, the cation and anion are assumed to have equal concentrations in both the base and perturbed states. Following a previous analysis [14], we introduce the electrochemical potential for the anion $\mu = \ln C - \Phi$ with $C = C^+ = C^-$. The base state electrical potential $\Phi = \ln C + V - 2\ln 2$ becomes singular as y tends to zero due to complete depletion, and this treatment avoids directly solving the electrical potential. The governing equations (1) become

$$\frac{\partial C}{\partial t} + \mathrm{Pe}(\boldsymbol{u} \cdot \nabla)C = \nabla^2 C, \tag{5a}$$

$$\frac{\partial C}{\partial t} + \mathrm{Pe}(\boldsymbol{u} \cdot \nabla)C = \frac{D+1}{2D}\nabla \cdot (C\nabla\mu), \tag{5b}$$

$$-\nabla p + \nabla^2 \boldsymbol{u} = 0, \quad \nabla \cdot \boldsymbol{u} = 0. \tag{5c}$$

The first two equations are linear combinations of the Nernst-Planck equations (1a) and (1b) for the cation and anion, and the third condition is the Stokes equations without the electric force. The boundary conditions become [14]

$$C|_{y=h} = 0, \quad (2\ln C - \mu)|_{y=2} = V + \ln C_s, \tag{6a}$$

$$\left.\frac{\partial \mu}{\partial y}\right|_{y=h,2} = 0, \tag{6b}$$

$$v|_{y=h} = \frac{1}{\mathrm{Pe}}\frac{\partial h}{\partial t}, \quad v|_{y=2} = 0, \tag{6c}$$

$$u|_{y=h} = -\frac{V^2}{8}\left.\frac{\frac{\partial^2 C}{\partial y \partial x}}{\frac{\partial C}{\partial y}}\right|_{y=h}, \quad u|_{y=2} = 2\ln 2\left.\frac{\partial \mu}{\partial x}\right|_{y=2}, \tag{6d}$$

$$(D+1)\left.\frac{\partial C}{\partial y}\right|_{y=h} - I = \frac{1}{v_m}\frac{\partial h}{\partial t}. \tag{6e}$$

In Eq. (6a), the first condition indicates that the anion is completely depleted from the anode surface, and the second condition represents the continuity of the chemical potential of the cation across the double layer near the cathode. Equation (6b) represents the zero-flux condition for anion on both electrodes. Equation (6c) is the same as its counterpart in (2c), the growth of the perturbed anode surface equals the normal velocity of the electrolyte, while the cathode surface is fixed in the moving frame of reference. In Eq. (6d), the first equation represents the second-kind osmotic slip velocity developed at the edge of the space charge layer near the anode, and the second equation represents the first-kind osmotic slip velocity at the edge of the equilibrium double layer near the cathode. Detailed derivations for the slip velocities are given in previous works [12,13]. Equation (6e), which is simplified from (2d) using the condition of equal migration and diffusion fluxes, indicates that the growth rate of the perturbed surface is caused by the perturbation in the cation flux.

As mentioned before, two types of problems will be considered in this section. The first problem is the purely EC instability with $h \equiv 0$ and the second problem is an interacting EC and Morph instability. The base state solutions for the two problems are exactly the same. In the rest of the paper, we use capital letters ($C^{\pm}$, M, and Φ) to represent the base solution, and small letters for the perturbed variables ($c^{\pm}$, μ, ϕ, u, v, and h). By directly solving Eq. (5), it is easy to find the base state of the ion concentration and chemical potential for anion is

$$C = y, \quad M = 2\ln 2 - V, \tag{7}$$

with limiting current $I = 2$.

We next perform a linear stability analysis to the base state solution. The ion concentration, chemical potential, and velocity are perturbed as $c = C + \epsilon c(y)e^{ikx+\sigma t}$, $\mu = M + \epsilon\mu(y)e^{ikx+\sigma t}$, $u = U_m y(2-y) + \epsilon u(y)e^{ikx+\sigma t}$, $v = \epsilon v(y)e^{ikx+\sigma t}$, and the anode surface $h = \epsilon h(y)e^{ikx+\sigma t}$, where $\epsilon \ll 1$ is a small perturbation. The perturbed governing equations are

$$\sigma c + ik\mathrm{Pe}U_m y(2-y)c + \mathrm{Pe}v = c'' - k^2 c, \tag{8a}$$

$$\sigma c + ik\mathrm{Pe}U_m y(2-y)c + \mathrm{Pe}v = \frac{D+1}{2D}(y\mu'' + \mu' - k^2 y\mu), \tag{8b}$$

$$v^{(4)} - 2k^2 v'' + k^4 v = 0, \tag{8c}$$

where the prime denotes the derivative with respect to y. k is the wave number, and σ is the complex eigenvalue whose real part σ_r determines the growth rate of the perturbation and whose imaginary part determines the wave speed $u_c = -\sigma_i/k$. The pressure-driven flow causes an ion advection along the flow direction. The perturbed boundary conditions on the two surfaces are

$$c(0) + h = 0, \quad c(2) - \mu(2) = 0, \tag{9a}$$

$$\mu'(0) = 0, \quad \mu'(2) = 0, \tag{9b}$$

$$v(0) = \frac{\sigma}{\mathrm{Pe}}h, \quad v(2) = 0, \tag{9c}$$

$$v'(0) = -\frac{V^2}{8}k^2c'(0), \quad v'(2) = 2\ln 2k^2\mu(2). \tag{9d}$$

$$c'(0) = \frac{\sigma}{(D+1)v_m}h. \tag{9e}$$

In the following, we will first discuss the purely EC instability and then the EC/Morph instability. For small or large ($k \ll 1$ or $k \gg 1$) wave numbers or when the perturbed flow is negligible ($v \ll 1$), we will analytically solve the equations (8). For arbitrary wave number k, the equations will be numerically solved using the Chebyshev collocation method [60].

A. Electroconvection problem

In this subsection, we consider the purely EC instability. We will first discuss the asymptotic solutions for the mode with the largest growth rate for $k \ll 1$, $k \gg 1$, and $v \ll 1$. Then, we show the results for arbitrary wave numbers by numerically solving Eqs. (8).

1. Small wave number, k ≪ 1

In the limit of small wave number ($k \ll 1$), the ion concentration and chemical potential are expanded as $c = c_0 + kc_1 + k^2c_2 + \cdots$ and $\mu = \mu_0 + k\mu_1 + k^2\mu_2 + \cdots$, the normal velocity $v = k^2v_2 + \cdots$ because of the slip velocity condition (9d), and the growth rate $\sigma = \sigma_0 + k\sigma_1 + k^2\sigma_2 + \cdots$. The leading order solutions are unaffected by the pressure-driven flow, and the results are given by Rubinstein *et al.* [14]:

$$c_0 = y, \quad \mu_0 = 2, \quad v_2 = \left(\frac{V^2}{16} + \left(\ln 2 - \frac{V^2}{32}\right)y\right)(y-2)y, \tag{10}$$

with the leading order growth rate $\sigma_0 = 0$. From the continuity equation $iku + v' = 0$, the slip velocity $u_s = u(0) = iV^2k/8$ is of order k. This is because the perturbation of the ion concentration occurs over the entire bulk region and it has an O(1) normal gradient. The perturbed tangential velocity is directly induced by the two slip velocities in opposite directions at the top and bottom surfaces and it creates fluxes of alternating signs normal to the channel surface by inducing EC vortices.

The effects of the pressure-driven flow arise in higher order equations. For each order, the basic steps are to first calculate c in terms of μ, then substitute it into Eq. (8b), and integrate the equation with boundary conditions (9b) to derive σ. In the end, the growth rate is found to be

$$\sigma = -\frac{2i}{3}\mathrm{Pe}U_mk + \left[\mathrm{Pe}\left(\frac{V^2 + 32\ln 2}{48}\right) - \frac{D+1}{D} - \frac{8}{945}\mathrm{Pe}^2U_m^2\right]k^2 + \cdots. \tag{11}$$

This result recovers the previous result [14] when $U_m = 0$. In the presence of the Poiseuille flow, the small wave-number perturbation propagates with the average fluid velocity $2\mathrm{Pe}U_m/3$, in which the prefactor Pe exists because time is scaled by L^2/D_0 instead of L/U_0. The growth rate is reduced at order k^2. The O(k) ion concentration and chemical potential are

$$c_1 = i\mathrm{Pe}U_m\left(\frac{D-4}{45(D+1)}y - \frac{y^3}{9} + \frac{y^4}{6} - \frac{y^5}{20}\right), \tag{12}$$

$$\mu_1 = -\frac{iD}{D+1}\mathrm{Pe}U_m\left(\frac{y^4}{8} - \frac{4y^3}{9} + \frac{y^2}{3}\right). \tag{13}$$

The asymptotic solution for $k \ll 1$ arises due to the finite distance between the two electrode surfaces. It can be either stable or unstable, depending on Pe, D, and U_m. The imposed flow always reduces the growth rate of the mode for $k \ll 1$. This result is consistent with the full analysis.

2. Negligible electroconvection, $v \approx 0$

Because of the pressure-driven flow, the EC velocity is negligible below a critical wave number. The eigenmode is solved by $c'' = [-a + a^2(y-1)^2]c$ with $a^2 = -ik\text{Pe}U_m$ and $\sigma + k^2 = a^2 - a$. The growth rate is

$$\sigma = -(k^2 + \sqrt{k\text{Pe}U_m/2}) + i(-k\text{Pe}U_m + \sqrt{k\text{Pe}U_m/2}); \tag{14}$$

i.e., this mode is always stable and its wave speed is the maximum fluid velocity $\text{Pe}U_m$. The ion concentration is

$$c = e^{-\sqrt{\text{Pe}kU_m/8}(y-1)^2(1-i)}, \tag{15}$$

which is a Gaussian distribution at the centerline of the channel. As we will see in the following, the full analysis has the exact solution for this mode. This center mode is always stable and it occurs below a transition wave number when the imposed flow is strong enough to overcome the electroosmotic slip velocity. Above the transition wave number, the electroosmotic slip velocity dominates the imposed flow and the EC instability is determined by the wall modes.

3. Large wave number, $k \gg 1$

For $k \gg 1$, the analysis is performed in the vicinity of the anode surface and the interelectrode distance can be considered as semi-infinite. Introducing the inner length scale $z = ky$ and considering the perturbations which decay away from the anode, i.e., $c(\infty) = v(\infty) = v'(\infty) = 0$, the perturbations are expanded as $c = c_0 + c_1/k + c_2/k^2 + \cdots$ and $\sigma = k^2\sigma_{-2} + k\sigma_{-1} + \sigma_0 + \cdots$. In the inner scale, the momentum equation (8c) becomes $v^{(4)} - 2v'' + v = 0$, where the prime now denotes the derivative with respect to z. Its solution is

$$v = k^2 z e^{-z}, \tag{16}$$

showing that the flow is induced by the slip velocity at the bottom surface only. From the continuity equation $iu + v' = 0$, the tangential velocity $u = iv'$ and the slip velocity

$$u_s = u(0) = ik^2. \tag{17}$$

At high wave number, the slip velocity is of order k^2 because the ion concentration disturbance is concentrated near the anode surface and has an O(k) normal gradient.

To calculate the growth rate, we need to solve the equations for the ion concentration. We find that σ_{-2} is not influenced by the imposed flow, $\sigma_{-1} = c_1 = 0$, σ_0 and σ_1 are purely imaginary, and one has to solve the fourth-order equation for σ_2 to see the effects of flow on the growth rate. The governing equations and the boundary conditions at each order are

$$c_0'' - (1 + \sigma_{-2})c_0 = \text{Pe}v_{-2}, \tag{18a}$$

$$c_1'' - (1 + \sigma_{-2})c_1 - \sigma_{-1}c_0 = 0, \tag{18b}$$

$$c_2'' - (1 + \sigma_{-2})c_2 - \sigma_{-1}c_1 - \sigma_0 c_0 = 2i\text{Pe}U_m z c_0, \tag{18c}$$

$$c_3'' - (1 + \sigma_{-2})c_3 - \sigma_{-1}c_2 - \sigma_0 c_1 - \sigma_1 c_0 = i\text{Pe}U_m(2zc_1 - z^2 c_0), \tag{18d}$$

$$c_4'' - (1 + \sigma_{-2})c_4 - \sigma_{-1}c_3 - \sigma_0 c_2 - \sigma_1 c_1 - \sigma_2 c_0 = i\text{Pe}U_m(2zc_2 - z^2 c_1), \tag{18e}$$

$$c_j(0) = c_j(\infty) = 0, \quad \text{for} \quad j \geqslant 0, \quad c_j'(0) = \begin{cases} -8/V^2, & \text{for} \quad j = 0, \\ 0, & \text{otherwise.} \end{cases} \tag{18f}$$

The above equations can be directly solved with the first two boundary conditions. Using the third boundary condition, one can then calculate the growth rate as

$$\sigma = \sigma_{-2}k^2 + \sigma_0 + \frac{\sigma_1}{k} + \frac{\sigma_2}{k^2} + \cdots, \tag{19}$$

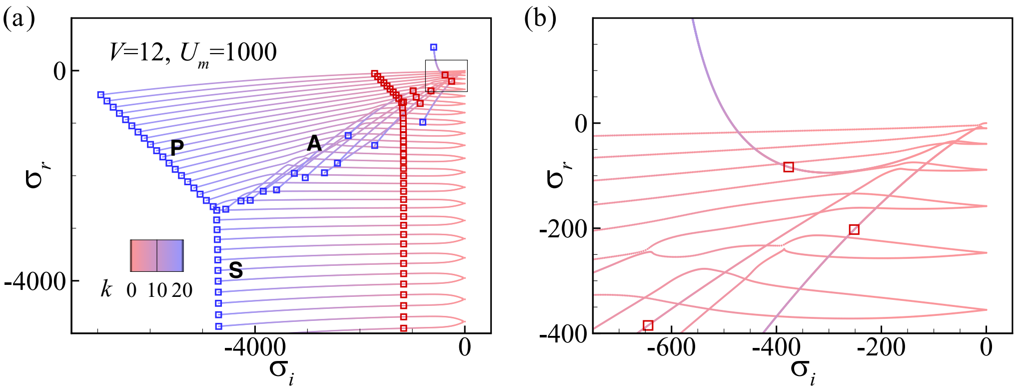

FIG. 3. (a) The spectrum of the purely EC instability in the range $0 \leqslant k \leqslant 20$ at $V = 12$ and $U_m = 1000$. The squares highlight the eigenvalues at two wave numbers $k = 5$ (red) and $k = 20$ (blue). (b) is a closer view of panel (a).

with

$$\sigma_{-2} = \frac{\mathrm{Pe}}{8}V^2 - \sqrt{\frac{\mathrm{Pe}}{2}}V, \tag{20a}$$

$$\sigma_0 = \frac{i\mathrm{Pe}U_m}{\sigma_{-2}\sigma_*}(3\sigma_* - 3 - 4\sigma_{-2}), \tag{20b}$$

$$\sigma_1 = \frac{i\mathrm{Pe}U_m}{2\sigma_0^2\sigma_*^3}\big[16(\sigma_* - 1) + \sigma_0(27\sigma_* - 35) + \sigma_0^2(12\sigma_* - 19)\big], \tag{20c}$$

$$\sigma_2 = \frac{\mathrm{Pe}^2U_m^2}{4\sigma_{-2}^3\sigma_*^5}\big[60(1 - \sigma_*) + \sigma_{-2}(179 - 149\sigma_*) + \sigma_{-2}^2(178 - 111\sigma_*) + \sigma_{-2}^3(59 - 24\sigma_*)\big], \tag{20d}$$

where σ_{-2} recovers the result without the imposed flow [12] and $\sigma_* = \sqrt{1 + \sigma_{-2}}$. In the presence of the pressure-driven flow, a perturbation of large wave number propagates with an $\mathrm{O}(1/k)$ wave speed and its growth rate is decreased by an $\mathrm{O}(1/k^2)$ term. The leading order ion concentration is

$$c_0 = -\frac{\mathrm{Pe}}{\sigma_{-2}^2}[2e^{-\sqrt{1+\sigma_{-2}}z} + (\sigma_{-2}z - 2)e^{-z}]. \tag{21}$$

The imposed flow reduces the growth rate of a perturbation at high wave numbers and the stabilizing effect becomes less effective as k increases. As we will see in the following, this result is consistent with the full analysis. The bulk analysis predicts that a full suppression of electroconvection by an imposed cross flow is impossible. This result is qualitatively different from what we will obtain from the full analysis.

4. Numerical results for all wave numbers

For arbitrary wave number, we apply a Chebyshev collocation method [60] to numerically solve Eqs. (8) and (9) for the eigensolutions. Figure 3(a) shows the eigenvalue spectrum for the purely EC instability for $0 \leqslant k \leqslant 20$, $V = 12$, and $U_m = 1000$ which corresponds to a velocity of 470 μm/s in a channel 2 mm wide. As in the high-Reynolds-number channel flow without electrokinetic effects, the spectrum has three branches of solutions. The A-branch solution of small wave speed corresponds to the wall mode, the P-branch solution of large wave speed corresponds to the center mode, and the S-branch solution is the highly damped mode whose wave speed is the average velocity $2\mathrm{Pe}U_m/3$. The P and S branches have very similar structures to those in

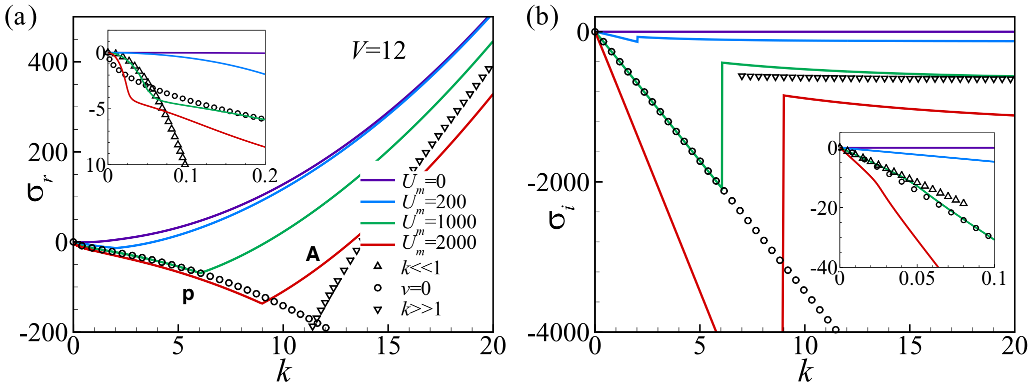

FIG. 4. The complex growth rate [(a) real; (b) imaginary] of the most unstable mode for the purely EC instability at different velocities at $V = 12$. The asymptotic solutions for $U_m = 1000$ are derived in Eqs. (11), (14), and (19) for $k \ll 1$, $v = 0$, and $k \gg 1$, respectively.

high-Reynolds-number channel flow without electrokinetic effects [61], indicating that the P and S modes are mainly caused by the parabolic velocity profile of the Poiseuille flow. The A branch is the mode which causes the EC instability. Figure 3(b) shows a closer view of the spectrum. At small wave number, all the modes are stable and the largest growth rate of the perturbations belongs to the P-branch solution. As the wave number increases, the growth rate of the center mode decreases while that of the wall mode increases, eventually resulting in an instability. This type of instability caused by the electroosmotic slip velocity is qualitatively different from the one in a channel flow due to inertial effects.

We now focus on the mode with the largest growth rate, which determines the linear instability of the flow. Figure 4 shows the eigenvalues of the most unstable mode as a function of the wave number k at $V = 12$. The symbols show the asymptotic solutions for $U_m = 1000$. For both real and imaginary parts of the growth rate, the abrupt changes in the curves manifest the transition from the centerline mode to the wall mode with increasing k, and the transition wave number k_{tr} increases with increasing velocity of the imposed flow. The centerline mode is always stable, while the wall mode eventually becomes unstable at large k, showing that the imposed flow can only suppress the electroconvection at large length scales. This effect is directly caused by the relative importance of the imposed flow and the second-kind electroosmotic slip velocity which causes the EC instability. The second-kind slip velocity is generated by the tangential gradient of the perturbed ion concentration [14] and is proportional to k^2. At small wave number, the slip velocity is negligible compared to the cross-flow and the linear instability is determined by the laminar channel flow. Therefore, the modes decay with $\sigma_r \sim -k^2$ due to the diffusion of the perturbed ion concentration. At sufficiently large wave numbers, the destabilizing effect of the slip velocity on the concentration field can always overtake the stabilizing effect due to the imposed flow and therefore leads to the EC instability. In Fig. 4(b), the centerline mode perturbation propagates downstream with a constant wave speed $u_c = -\sigma_i/k = \text{Pe}U_m$ which is exactly the velocity of the imposed flow at the centerline. The wall mode perturbation has a smaller wave speed $u_c \sim 1/k$, indicating that near the wall the small vortices propagate more slowly than the large vortices.

To examine the manner in which modes are stabilized by the imposed flow, we compare the eigenfunctions of the most dangerous mode at different velocities in Fig. 5. The results are normalized such that the magnitude of the ion concentration has the same maximum value $c_{\max} = 1$. At $V = 12$ and $k = 8$, the perturbations grow at $U_m = 0$ and decay at $U_m = 1000$ and 2000. At a sufficiently high flow rate $U_m = 2000$, the perturbed ion concentration has a Gaussian distribution at the centerline of the channel. The ion concentration gradients at the two walls are small and

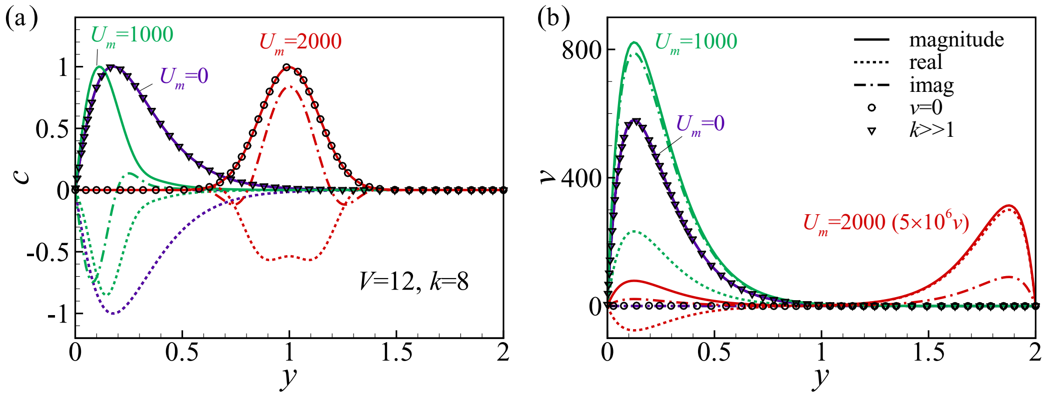

FIG. 5. Distribution of the perturbed (a) ion concentration and (b) normal velocity of the most unstable mode for the EC instability at $U_m = 0$, 1000, and 2000, for $V = 12$ and $k = 8$. Perturbations grow at $U_m = 0$ and decay at $U = 1000$ and 2000. The velocity for $U_m = 2000$ is multiplied by 5×10^6. Symbols show the magnitude of the analytical solutions for $v = 0$ and $k \gg 1$ given in Eq. (15) and Eqs. (16) and (21), respectively.

therefore the induced electroosmotic slip velocities are negligible on both sides. Note that the velocity for $U_m = 2000$ has been multiplied by 5×10^6 for clarity. In comparison, at $U_m = 0$ the ion concentration has a large perturbation at the anode surface and induces a strong slip velocity at the bottom of the channel. The real components of c and v have opposite signs near $y = 0$. This means that the increase of the ion concentration generates a local downward flow which flushes more ions into this region and further amplifies the perturbation. At $U_m = 1000$, the perturbations are concentrated near the bottom surface. The magnitude of the velocity v is higher than in the case with $U_m = 0$, while the real part is smaller, showing that the imposed flow suppresses the instabilities by reducing the coupling between the electroosmotic slip velocity and the ion concentration gradient.

The marginal stability curves in the $k - V$ space at different imposed velocities are compared in Fig. 6(a). At $U_m = 0$, the critical voltage for the pure EC instability is $V_{\mathrm{cr}1} = \sqrt{48(1 + 1/D)/\mathrm{Pe} - 32 \ln 2} = 14.4$ for $k \ll 1$ and $V_{\mathrm{cr}2} = \sqrt{32/\mathrm{Pe}} = 9.6$ for $k \gg 1$. As shown in the previous results, the imposed flow only increases the critical voltage at small wave number, while

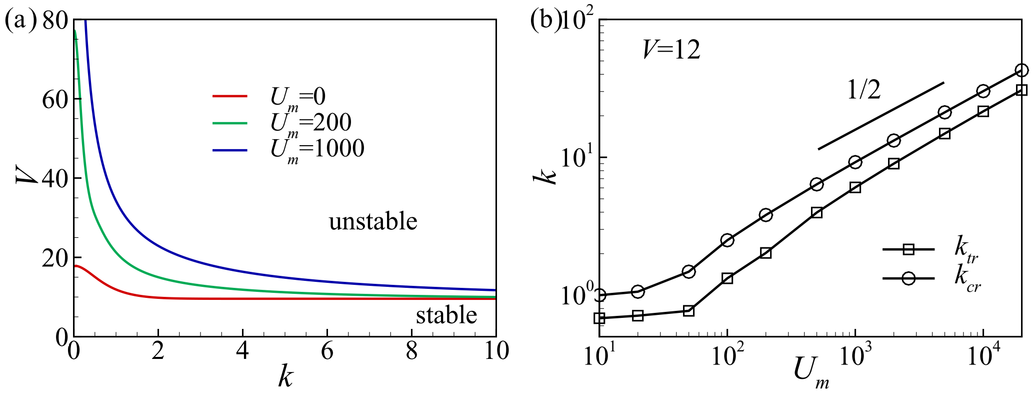

FIG. 6. (a) The marginal stability curves in the $k - V$ space at different cross-flow velocities. (b) The dependence of k_{cr} and k_{tr} on U_m at a constant potential $V = 12$. k_{cr} is the critical wave number at which the mode becomes unstable; k_{tr} is the transition wave number between centerline and wall modes and has the minimum growth rate.

at large k, all the curves reach the same critical voltage. At a fixed voltage, increasing the velocity U_m increases the critical wave number k_{cr} at which the mode becomes unstable. In Fig. 6(b), both the critical wave number k_{cr} and the transition wave number between the two modes k_{tr} increase as $U_m^{1/2}$ at large U_m, suggesting that the electroconvection is stabilized when the concentration field is more influenced by the imposed flow U_m than the electroosmotic slip velocity $u_s \sim k^2 V^2$. As we will see in Sec. IV C, in order to suppress the EC instability, the imposed flow has to overcome the perturbed EC velocity and distort the concentration field, causing a sheltering effect. To summarize, the bulk analysis predicts that the pressure-driven flow can attenuate the small wave-number modes that would arise in a pure EC instability, and the critical wave number above which modes are suppressed increases with flow speed as $k_{\mathrm{cr}} \sim U_m^{1/2}$.

B. Electroconvection/morphological problem

In this subsection, we consider the interaction between EC and Morph instabilities. In contrast to the pure EC instability, the EC/Morph instability is always unstable. In the following, we will first discuss the asymptotic solutions for $k \ll 1$ and $k \gg 1$, and then show the numerical result for arbitrary wave number. We also want to point out that the purely Morph instability occurs even at underlimiting currents. The growth rate in this case follows the same expression as the current result except that the current I replaces the limiting current $I_{\mathrm{lim}} = 2$.

1. Small wave number, k ≪ 1

For $k \ll 1$, the variables are expanded as $c = c_0 + kc_1 + \cdots$, $\mu = \mu_0 + k\mu_1 + \cdots$, $v = v_0 + kv_1 + \cdots$, and $\sigma = \sigma_0 + k\sigma_1 + \cdots$. Unlike the purely EC instability, here the velocity v is directly caused by the growth of the electrode surface and its leading term is O(1) instead of O(k^2). Therefore, the two highest order equations are $v_j^{(4)} = 0$ with boundary conditions $v_j(0) = \sigma_i h/\mathrm{Pe}$ and $v_j'(0) = v_j(2) = v_j'(2) = 0$ for $j = 0, 1$. The solutions are

$$v_j = \frac{(y+1)(y-2)^2}{4\mathrm{Pe}}\sigma_j h, \quad \text{for} \quad j = 0, 1. \tag{22}$$

For the ion concentration, the leading order equation and the boundary conditions are

$$\sigma_0 c_0 + \mathrm{Pe} v_0 = c_0'', \tag{23a}$$

$$c_0(0) + h = 0, \quad c_0'(0) = \frac{\sigma_0 h}{(1+D)v_m}, \tag{23b}$$

leading to the solution

$$c_0 = \left(\frac{\sqrt{\sigma_0}h}{(1+D)v_m} + \frac{3h}{2\sqrt{\sigma_0^3}}\right)\sinh(\sqrt{\sigma_0}y) - \frac{h}{4\sigma_0}[6\cosh(\sqrt{\sigma_0}y) + 6(y-1) + (y+1)(y-2)^2\sigma_0]. \tag{24}$$

Combining the equations for ion concentration and chemical potential, and using the boundary conditions $\mu_0'(0) = \mu_0'(2) = 0$, one can derive $c_0'(2) = c_0'(0)$ and find the leading order growth rate at $k = 0$,

$$\sqrt{\sigma_0}\coth\sqrt{\sigma_0} = 1 + \frac{2\sigma_0^2}{3(1+D)v_m}, \tag{25}$$

where $D = D^+/D^-$ is the ratio of the cation and anion diffusivities, and $v_m = 0.013$ is the dimensionless molar volume of the lithium metal. In typical electrolytes, $D \approx 1$ and $v_m \ll 1$, the growth rate $\sigma_0 \ll 1$. Using the approximation $\sqrt{\sigma_0}\coth\sqrt{\sigma_0} \simeq 1 + \sigma_0/3$, we get $\sigma_0 \simeq (D+1)v_m/2$ for $v_m \ll 1$, and the ion concentration $c_0 \simeq h(y/2 - 1)$.

As a comparison, the growth rate for the purely EC instability is $\sigma = 0$ at $k = 0$. On the other hand, the growth rate for the purely Morph instability follows:

$$\coth\sqrt{\sigma_0} = \frac{\sqrt{\sigma_0}}{(1+D)v_m}, \tag{26}$$

and the approximate solution is $\sigma_0 \simeq (D+1)v_m$ and $c \simeq h(y-1)$ for $v_m \ll 1$. The Morph instability is intrinsically unstable even at $k = 0$. This result can be understood from the boundary condition at the electrode surface. Consider a local peak on the anode surface: The boundary condition $c(0) + h = 0$ reduces the ion concentration at the surface and enhances the ion flux by increasing the local concentration gradient, thereby causing more deposition. Allowing the EC effect smooths the ion concentration gradient at $y = 0$ and reduces the growth rate by half. This is the leading order growth rate of the perturbation, which is not affected by the pressure-driven flow.

The pressure-driven flow affects the eigenvalue at higher orders. Here we only consider the next order solution with $v_m \ll 1$, for which the eigenvalue

$$\sigma_1 \simeq 2i\mathrm{Pe}U_m/3 \tag{27}$$

is purely imaginary. Like the purely EC mode, the Morph perturbation at small k has a wave speed equal to the average fluid velocity. However, its propagation is in the opposite direction, against the imposed flow. This is because the cross flow brings more ions to the windward side of a perturbed surface, increases the local deposition on this side, and therefore causes the wave to propagate upstream. Since the applied flow suppresses the electroconvection, we expect the pressure-driven flow to increase the growth rate for the EC/Morph instability for $k \ll 1$.

2. *Large wave number, $k \gg 1$*

For $k \gg 1$, the analysis is performed in the vicinity of the depletion anode surface with an inner scale $z = ky$ and the electrolyte is considered to be semi-infinite. In our previous study on the bulk region [41], we derived the analytical solution for $k \gg 1$ without a flow. The growth rate monotonically increases with the wave number k, and its scaling depends on the applied voltage. For $V < V_{\mathrm{cr2}}$, where $V_{\mathrm{cr2}} = \sqrt{32/\mathrm{Pe}}$ is the critical voltage for the onset of electroconvection for $k \gg 1$, the growth rate $\sigma \sim k$. For $V > V_{\mathrm{cr2}}$, the instability is mainly contributed by the EC instability and $\sigma \sim k^2$. The growth rate for the coupled instability in an imposed flow has the same scalings.

For $V < V_{\mathrm{cr2}} = \sqrt{32/\mathrm{Pe}}$, we have

$$\sigma = k\sigma_{-1} + \sigma_0 + \frac{\sigma_1}{k} + \cdots, \tag{28}$$

with

$$\sigma_{-1} = \frac{(D+1)v_m}{1 - \mathrm{Pe}V^2/32}, \tag{29a}$$

$$\sigma_0 = -256(D+1)^2 v_m^2 \frac{1 + \mathrm{Pe}V^2/32}{(1 - \mathrm{Pe}V^2/32)^3}, \tag{29b}$$

$$\sigma_1 = \frac{(D+1)^3 v_m^3}{16}\frac{3 + 5\mathrm{Pe}V^2/32}{(1 - \mathrm{Pe}V^2/32)^5} + \frac{i(D+1)v_m\mathrm{Pe}U_m}{4}\frac{2 - 7\mathrm{Pe}V^2/32}{(1 - \mathrm{Pe}V^2/32)^2}. \tag{29c}$$

The imposed flow reduces the growth rate of the EC/Morph instability at high wave numbers. The wave speed of the perturbation scales as $u_c = \sigma/k \sim \mathrm{O}(k^{-2})$; the wave can propagate either downstream or upstream depending on the applied voltage.

The leading order solutions for the ion concentration and normal velocity are

$$c = -he^{-z} + \frac{\mathrm{Pe}V^2 h}{32 - \mathrm{Pe}V^2} z(z+1)e^{-z}, \tag{30a}$$

$$v = -\frac{k^2 h}{8 - \mathrm{Pe}V^2/4} ze^{-z}. \tag{30b}$$

Note that the normal velocity boundary condition $v(0) = \sigma h/\mathrm{Pe}$ does not affect the leading order equation since $\sigma \sim k$ has a smaller order than the normal velocity $v \sim k^2$. In other words, the growth of the anode surface makes a negligible contribution to the fluid velocity. Instead, the flow is mainly induced by a tangential electroosmotic slip velocity (9d) due to the ion concentration gradient caused by the surface perturbation.

As a comparison, the growth rate for the purely Morph instability at $k \gg 1$ is [41]

$$\sigma = (D+1)v_m k \tag{31}$$

and the perturbed ion concentration is

$$c = -he^{-z}. \tag{32}$$

At large wave number, the electroosmotic slip flow increases the growth rate of the Morph instability, even before the onset of electroconvection. This is because the electroosmotic flow near the electrode surface increases the ion concentration gradient and therefore enhances the instability. This result is opposite to the growth rate at small wave number, for which the electroconvection reduces the growth rate of the Morph instability.

For $V > V_{\mathrm{cr}2}$, the instability is dominated by electroconvection and the growth rate is

$$\sigma = k^2 \sigma_{-2} + \cdots, \tag{33}$$

with $\sigma_{-2} = \mathrm{Pe}V^2/8 - \sqrt{\mathrm{Pe}V^2/2}$, which is the same as for the purely EC instability in Eq. (20a).

The leading order solutions for ion concentration and velocity are

$$c = \frac{\mathrm{Pe}V^2 kh}{8(D+1)v_m \sigma_{-2}} \left[2e^{-\sqrt{\sigma_{-2}+1}z} + (\sigma_{-2}z - 2)e^{-z}\right], \tag{34a}$$

$$v = -\frac{\sigma_{-2}V^2 k^3 h}{8(D+1)v_m} ze^{-z}, \tag{34b}$$

which are the same as Eqs.. (16) and (21) for the purely EC instability.

3. Numerical results for all wave numbers

Figure 7(a) shows the growth rate of the most unstable mode for the purely EC instability, the purely Morph instability, and the coupled instability. For the Morph instability, the growth rate is independent of the applied potential since the base state current is a constant $I = 2$. Its growth rate scales as $\sigma_r \sim (D+1)v_m$ for $k \ll 1$ and $\sigma_r \sim (D+1)v_m k$ for $k \gg 1$, and it has a minimum growth rate at $k \approx 0.3$. Allowing the EC instability decreases the growth rate for small k while increasing it for large k. The pressure-driven flow reduces the effects of electroconvection, it increases the growth rate of the perturbation for small k, and it decreases the growth rate for $k > 1$, but eventually its effect becomes negligible. In Fig. 7(b), the perturbation becomes a traveling wave even without the onset of the electroconvection due to a nonuniform deposition on the upwind and downwind sides of the perturbation, and it propagates upstream at small k and downstream at large k. The electroconvection substantially increases the wave speed of the perturbation at large k.

The imposed flow stabilizes the base state for the coupled instability problem mainly through mitigating the electroconvection. Figure 8 shows the eigenfunctions of the most unstable mode for $V = 12$ and $k = 3$ at $U_m = 0$, for which EC instability occurs, and $U_m = 200$, for which electroconvection is suppressed by the imposed flow. The amplitude of the perturbed electrode

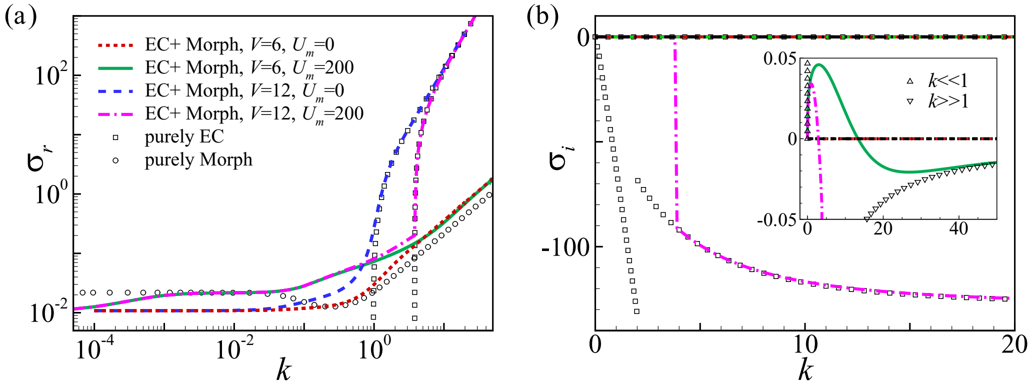

FIG. 7. The maximum growth rate [(a) real; (b) imaginary] of the EC, Morph, and the coupled instabilities with and without the cross flow. The asymptotic solutions of σ_i for $k \ll 1$ and $k \gg 1$ are given in Eqs. (27) and (29c), respectively.

surface is $h = 1$. In both cases, the local peak of the anode surface causes a downward flow and an enhanced ion concentration gradient which brings more ions to the peak and amplifies the instability. This result is consistent with previous experimental observations that the flow converges at the tips of the dendrites [24]. The cross flow greatly reduces the ion concentration gradient and the velocity of the downward flow, therefore reducing the growth rate of the Morph instability.

IV. FULL ANALYSIS

A. Method

So far, we have considered the linear instability of the bulk region, assuming electroneutrality and using the second-kind electroosmotic slip velocity to replace the thin space charge layer. This simplification allows us to analytically derive the asymptotic solutions for small and large wave numbers. The bulk analysis predicts that the imposed flow cannot completely suppress the EC instability because the ion concentration disturbance caused by the slip velocity $u_s \sim k^2V^2$ will always dominate the stabilizing effect by the imposed flow at large wave numbers. However, the

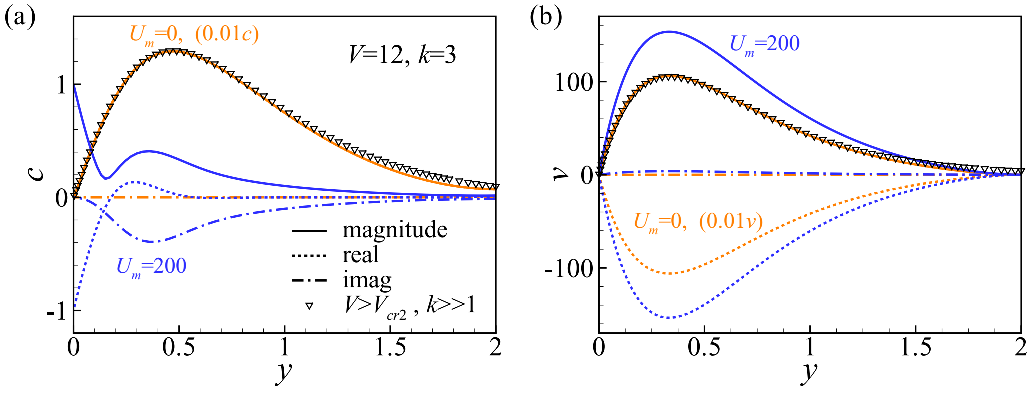

FIG. 8. Distribution of the perturbed (a) ion concentration and (b) normal velocity for the most unstable mode of the EC/Morph instability at $U_m = 0$ and 200, $V = 12$, $k = 3$. The results for $U_m = 0$ are multiplied by 0.01. Symbols show the high-wave-number asymptotic solutions (34).

TABLE I. Comparison of the largest growth rates at different k for the EC instability derived using the ultraspherical spectral method and the shooting method, $\delta = 10^{-3},\ V = 25,\ \mathrm{Pe} = 0.35,\ D = 2/3$, and $V_m = 0$.

k	Ultraspherical spectral method	Shooting method
0.1	-0.016096836493756	-0.016096836696248
1	1.279100815430633	1.279100816345562
10	$1.103806945236518 \times 10^2$	$1.103806944029065 \times 10^2$
100	$-9.996152401785079 \times 10^3$	$-9.996152401758340 \times 10^3$

assumption of thin space charge layer in the bulk analysis is no longer valid at high wave numbers and it incorrectly predicts an infinite growth rate $\sigma \sim k^2$ as $k \to \infty$ for the EC instability [15]. To understand the effects of the imposed flow on modes at high wave numbers, we now consider the linear instability of the full region, which includes the double layer and the space charge layer, and we no longer assume electroneutrality. In the full analysis, the base state is derived by numerically solving Eqs. (3) and (4). The eigenmodes are then calculated by solving the perturbed equations

$$\sigma c^+ + ik\mathrm{Pe}U_m y(2-y)c^+ + \mathrm{Pe}vC^{+\prime} = \frac{D+1}{2}[c^{+\prime\prime} - k^2c^+ - k^2C^+\phi + (C^+\phi' + c^+\Phi')'], \tag{35a}$$

$$\sigma c^- + ik\mathrm{Pe}U_m y(2-y)c^- + \mathrm{Pe}vC^{-\prime} = \frac{D+1}{2D}[c^{-\prime\prime} - k^2c^- + k^2C^-\phi - (C^-\phi' + c^-\Phi')'], \tag{35b}$$

$$2\delta^2(\phi'' - k^2\phi) = c^- - c^+, \tag{35c}$$

$$v^{(4)} - 2k^2v'' + k^4v = k^2((\phi'' - k^2\phi)\Phi' - \phi\Phi^{(3)}), \tag{35d}$$

with boundary conditions

$$(c^+ + C^{+\prime}h)|_{y=0} = 0, \quad c^+|_{y=2} = 0, \tag{36a}$$

$$(c^{-\prime} - C^-\phi' - c^-\Phi')|_{y=0,2} = 0, \tag{36b}$$

$$(\phi + \Phi'h)|_{y=0} = 0, \quad \phi|_{y=2} = 0, \tag{36c}$$

$$v|_{y=0} = \frac{\sigma h}{\mathrm{Pe}}, \quad v|_{y=2} = 0, \quad v'|_{y=0,2} = 0, \tag{36d}$$

$$\frac{1+D}{2}(c^{+\prime} + C^+\phi' + c^+\Phi')|_{y=0} = \frac{\sigma h}{v_m}. \tag{36e}$$

Both the base state and the perturbed equations are solved using the ultraspherical spectral method [59]. In contrast to the classical Chebyshev collocation method [60], this method constructs the matrices in the coefficient space and uses banded operators to greatly reduce the condition number of the matrices. This allows inclusion of more Chebyshev coefficients to fully resolve the thin double layers. For the generalized eigenvalue problem, the ultraspherical spectral method is accurate up to around 6000 coefficients, while the classical Chebyshev collocation method becomes ill conditioned with more than 100 collocation points. To validate the current method, we first consider the EC instability of the full region without a flow. Table I shows that the largest growth rates at different k for the EC instability derived by the ultraspherical spectral method and the shooting method for $\delta = 10^{-3}$, $V = 25$ and $V_m = 0$ are nearly identical. Figure 9 compares the marginal stability curves obtained with the ultraspherical method to those from a previous study that used a shooting method [15]. Here $\mathrm{Pe} = 0.5$, $D = 1$, and $U_m = 0$. The two results agree well with each other. The small differences are probably because in Ref. [15] the equilibrium double layer near the top electrode surface is modeled with the first-kind electroosmotic slip velocity, while here it is fully resolved. We also compared our result with a previous linear stability analysis based on an unsteady base state for $V = 50,\ \delta = 1.414 \times 10^{-3}$, and $U_m = 0$ [62]. Both studies predict the same wave number for

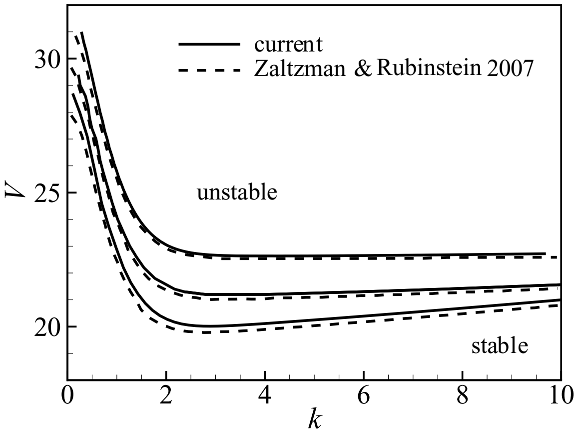

FIG. 9. The marginal stability curves for the purely EC instabilities with different double layer thickness, $\mathrm{Pe} = 0.5$, $D = 1$, and $U_m = 0$. From bottom to top: $\delta = 3\sqrt{2} \times 10^{-4}$, $\sqrt{2} \times 10^{-4}$, and $3\sqrt{2} \times 10^{-5}$. The solid lines are obtained with the ultraspherical method. The dashed lines show the results from Ref. [15].

the most unstable mode, confirming the validity of the quasisteady approximation of the base state in this study.

B. Electroconvection without imposed flow

Before considering the effects of the imposed flow, we first compare the EC instabilities derived from the bulk and full analysis. Figure 10(a) shows the largest growth rate of the purely EC instability with different δ at $U_m = 0$. At $V = 25$, the full analysis predicts stable modes at small ($k < k_1$) and large ($k > k_2$) wave numbers and unstable modes in between. At $V = 25$, the bulk analysis predicts unstable modes at all wave numbers since the voltage is above the critical voltages

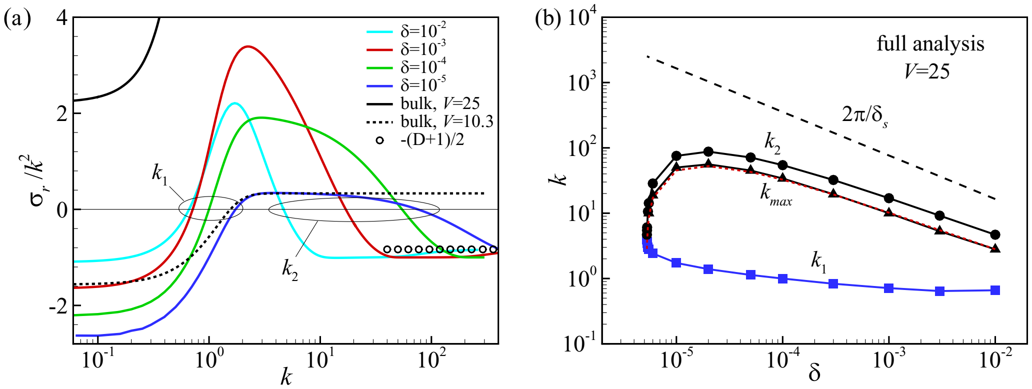

FIG. 10. (a) The dependence of the growth rate σ_r/k^2 on the wave number k for the purely EC instability at $U_m = 0$, $\mathrm{Pe} = 0.35$, and $D = 2/3$. Colored lines: full analysis at $V = 25$ for different double-layer thicknesses. Black lines: bulk analysis at different voltages. The solid black line ($V = 25$) reaches $\sigma_r/k^2 = 16.89$ at large k, while the dotted line ($V = 10.3$) has better agreement with the full analysis at $\delta = 10^{-5}$ for $1 < k < 10$. k_1 and k_2 represent the two wave numbers at which the growth rate becomes zero. Open circles show the asymptotic solution $\sigma_r = -(D + 1)k^2/2$ as $k \to \infty$. (b) The dependence of k_1, k_2, and $k_{\max}$ on δ for the full analysis at $V = 25$. The red dotted line shows the result of $0.6k_2$. The dashed line shows the corresponding wave number of the space charge layer, $\delta_s = (9\delta^2V^2/8)^{1/3}$.

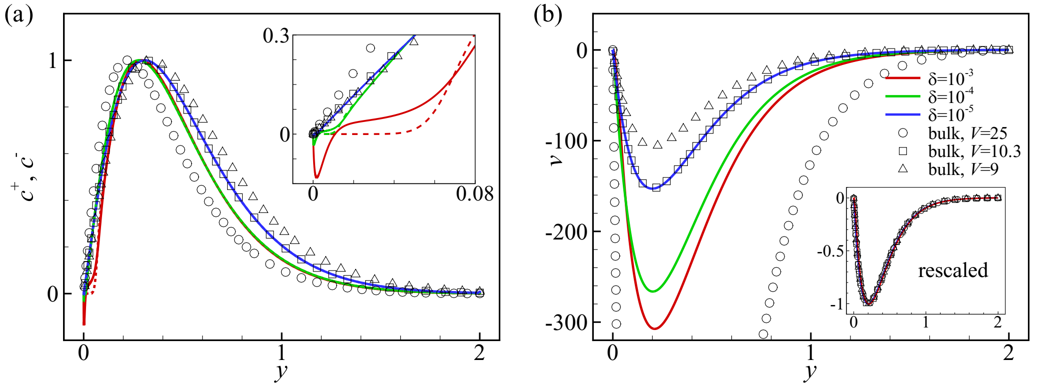

FIG. 11. The perturbed (a) ion concentration (solid, cation; dashed, anion) and (b) velocity for the EC instability at $U_m = 0$ and $k = 5$. Lines: full analysis at $V = 25$. Symbols: bulk analysis at different voltages.

$V_{\text{cr1}} = 14.4$ for $k \ll 1$ and $V_{\text{cr2}} = 9.6$ for $k \gg 1$. Its predicted growth rates $\sigma_r = 2.22k^2$ for $k \ll 1$ and $\sigma_r = 16.89k^2$ for $k \gg 1$ are much larger than those from the full analysis at the same voltage. One reason for this result is that the bulk analysis neglects the $\mathrm{O}(\ln \delta)$ potential drop inside the double layer and space charge layer [13] and therefore overestimates the slip velocity. Reducing the voltage to smaller values decreases the growth rate for the bulk analysis. For example, adjusting the voltage to $V = 10.3$ brings the bulk analysis for $1 < k < 10$ closer to the full analysis for $\delta = 10^{-5}$ as shown in Fig. 13. Later, we will see that these two analyses also have similar eigenfunctions. The bulk analysis at $V = 10.3$ still quickly deviates from the full analysis at large k and predicts an infinite growth rate as $k \to \infty$. The deviation occurs at a wave number which is smaller than the inverse of the space charge layer $\varepsilon \sim (\delta V)^{2/3}$ [14], showing that the linear instability of the mode is strongly influenced by the space charge layer. For $k < k_1$ and $k > k_2$, the full analysis predicts a stable mode with $\sigma_r \sim -k^2$, indicating that the mode is stabilized by diffusion of the ions inside the space charge layer. As $k \to \infty$, $\sigma_r \sim -(D + 1)k^2/2$. For an intermediate range of wave numbers, $k_1 < k < k_2$, the full analysis predicts an unstable mode whose growth rate scales as $\sigma_r \sim k^2$ due to the scaling of the electroosmotic slip velocity. The result is more evident at smaller δ and larger V, where the perturbation is unstable over a larger range of wave numbers. To better understand the transitions between stable and unstable modes, we plot k_1 and k_2 as functions of δ at $V = 25$ in Fig. 10(b). The result is composed of two regions. At large δ, the applied voltage $V = 25$ is well above the critical voltage for the onset of the EC instability. $k_1 \sim \mathrm{O}(1)$, and it slightly increases with decreasing δ, suggesting that the stabilization of the modes at small wave numbers is related to the gap between the two electrode surfaces. k_2 roughly scales as $\delta^{-2/3}$, meaning that the modes are stabilized due to the space charge layer whose thickness is $\delta_s = (9\delta^2 V^2/8)^{1/3}$ [29]. This stabilization cannot be captured by the bulk analysis. At smaller δ, when the applied voltage $V = 25$ is close to the critical voltage, k_1 and k_2 change more rapidly with decreasing δ and eventually $k_1 = k_2$, reaching the critical wave number for neutral instability. At small δ, k_1 and k_2 do not follow a simple scaling law with the gap thickness or the space charge layer thickness, probably because the potential drop across the double layer and space charge layer has a large effect. The wave number of the most unstable mode $k_{\max} \approx 0.6k_2$.

The similarities between the bulk and full analyses for $k < k_2$ are further illustrated through their eigenfunctions in Fig. 11. Here, we compare the profiles of ion concentrations c^+, c^-, and normal velocity v at $k = 5$. The eigenfunctions are normalized such that the ion concentrations have the same peak value of $c^+_{\max} = 1$. The overall distribution of the perturbed ion concentration is not sensitive to the specific values of δ or V in Fig. 11(a). However, the ion concentration distribution and its gradient near the space charge layer, which determines the slip velocity and the EC instability,

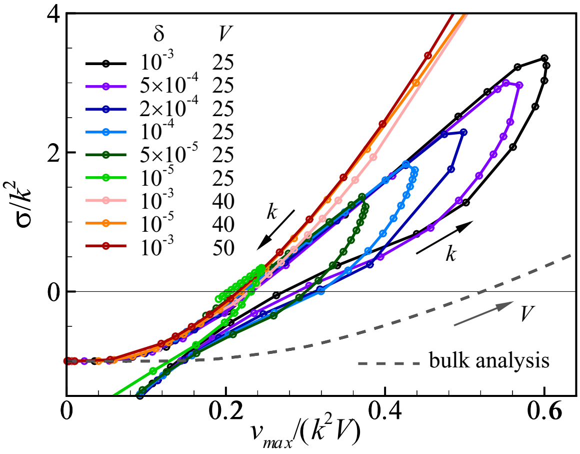

FIG. 12. The dependence of σ_r/k^2 on $v_{\max}/(k^2V)$. $v_{\max}$ is the maximum normal velocity when the perturbed ion concentration has the peak value $c^+_{\max} = 1$. Symbol lines show the full analysis results, where each individual symbol corresponds to a specific wave number k. Increasing k, the transitions from stable to unstable then to stable modes again correspond to the wave numbers k_1 and k_2, respectively. Dotted line shows the bulk analysis results at $k = 50$ with the voltage V increasing from left to right. The bulk analysis is derived from Eqs. (16), (20a), and (21).

is strongly dependent on δ and V. In the full analysis, the variation of the cation ion concentration in the space layer at $y = 0$ decreases with decreasing δ. Since the velocity field is driven by $(c^- - c^+)/\delta^2$, the effects of the space charge layer on the ion concentration is not negligible even at small δ. The magnitude of the slip velocity and the instability is determined by the slope of the ion concentration outside the space charge layer. The bulk analysis at $V = 25$ overestimates its gradient near $y = 0$ and therefore leads to a much larger velocity that causes a larger growth rate. By reducing the voltage to $V = 10.3$, the ion concentration and velocity profiles agree well with the full analysis results for $\delta = 10^{-5}$, leading to a closer agreement of the growth rate as well. All the velocities follow the same relation $v \sim ye^{-ky}$, meaning that the EC instability is driven by osmotic slip velocities of the same form but with different magnitudes.

For the unstable mode, the bulk analysis can be made quantitatively comparable with the full analysis by adjusting the voltage. However, the bulk analysis cannot predict the transition from an unstable to a stable mode with increasing k. To better understand this transition at $k = k_2$, we plot the rescaled growth rate σ_r/k^2 as a function of $v_{\max}/(k^2V)$ in Fig. 12. Since the eigenfunctions can be multiplied by any constant without affecting the result, we normalized the eigenfunctions such that the ion concentration has the peak value $c^+_{\max} = 1$. The symbol lines show the results of the full analysis and each individual point represents a specific wave number k. The growth rate strongly depends on the magnitude of the rescaled velocity $v_{\max}/(k^2V)$. The transition from stable to unstable mode at k_1 depends on δ and V. For $\delta \geqslant 5 \times 10^{-5},\ V = 25$, it occurs at $v_{\max}/(k^2V) \simeq 0.3 \pm 0.02$; for $\delta = 10^{-5},\ V = 25$, which is closer to the neutral stability, it occurs at $v_{\max}/(k^2V) \simeq 0.23$; and at higher voltages, all small wave-number perturbations are unstable and k_1 does not exist. In comparison, the transition from unstable to stable mode at k_2 always occurs at $v_{\max}/(k^2V) \simeq 0.21 \pm 0.01$. This result shows that the EC instability is suppressed if the normal velocity is not strong enough to overcome the ion diffusion and sustain the ion flux from low- to high-concentration regions. The bulk analysis only shows the transition at k_1. It overestimates the transition velocity $v_{\max}/(k^2V) = (\sqrt{5} - 2)e^{(\sqrt{5}-1)/2}/\sqrt{2\mathrm{Pe}} = 0.52348$, where the numerical factor is calculated from the bulk analysis prediction for $k \gg 1$. This is because it underpredicts the voltage for the onset of the EC instability [15].

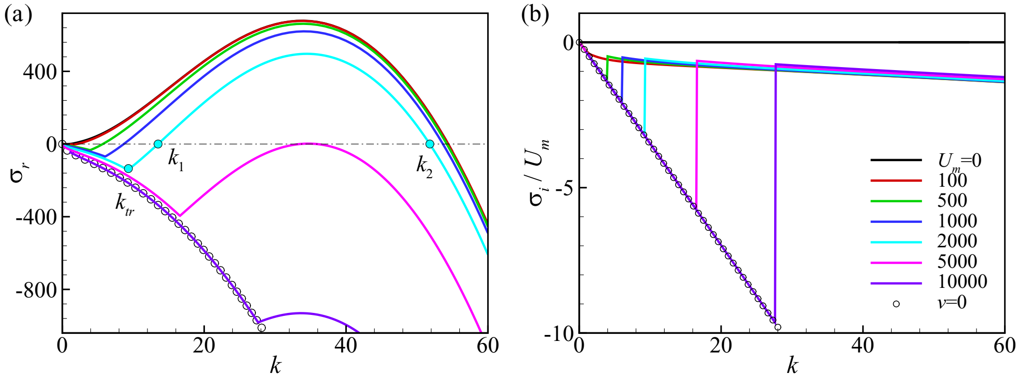

FIG. 13. The (a) real and (b) imaginary parts of the maximum growth rate of the purely EC instability at different U_m for $\delta = 10^{-4}$ and $V = 25$. Symbols show the analytical solution for $v = 0$ given in Eq. (14). $k_{\rm tr}$ is the transition wave number between the centerline and wall modes. k_1 and k_2 are the wave numbers for zero growth rate.

C. Effect of imposed flow on electroconvection

We now consider the effects of the cross flow on the EC instability. Figure 13 shows the complex eigenvalue σ as a function of k at different U_m, $\delta = 10^{-4}$ and $V = 25$. Below the transition wave number $k_{\rm tr}$, the perturbation is stable and it propagates downstream with the velocity at the channel centerline PeU_m. The eigenvalue of the mode follows the same asymptotic solution (14) in the bulk analysis. Above $k_{\rm tr}$, the EC instability is determined by the wall mode, which has a local maximum growth rate at $k \simeq 34$ and the wave speed roughly follows $u_s \sim 1/k$. The predictions of the bulk [see Fig. (4)] and full analyses for the complex growth rate at relatively small wave numbers are very similar to one another. Increasing U_m delays the transition from the center mode to the wall mode and reduces the peak value of the growth rate. At a fixed voltage, we also find the transition wave number scales as $k_{\rm tr} \sim U_m^{1/2}$ as in the bulk analysis. In the full analysis, full suppression of the EC instability is possible in a strong enough flow. This result is qualitatively different from the bulk analysis.

Figure 14(a) shows the marginal stability curves at different imposed velocities U_m for $\delta = 10^{-4}$. The imposed flow stabilizes the modes at small wave numbers, while it does not affect the transition

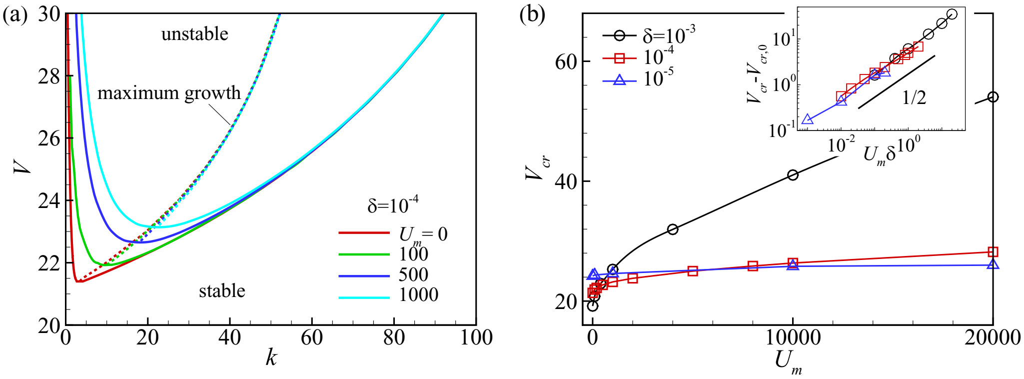

FIG. 14. (a) Marginal stability curves for the purely EC instability at different U_m, $\delta = 10^{-4}$. (b) Dependence of the critical voltage $V_{\rm cr}$ on the velocity of the cross flow U_m at different double-layer thicknesses. The inset shows that the increment of the critical voltage scales as $V_{\rm cr} - V_{\rm cr,0} \sim (U_m\delta)^{1/2}$.

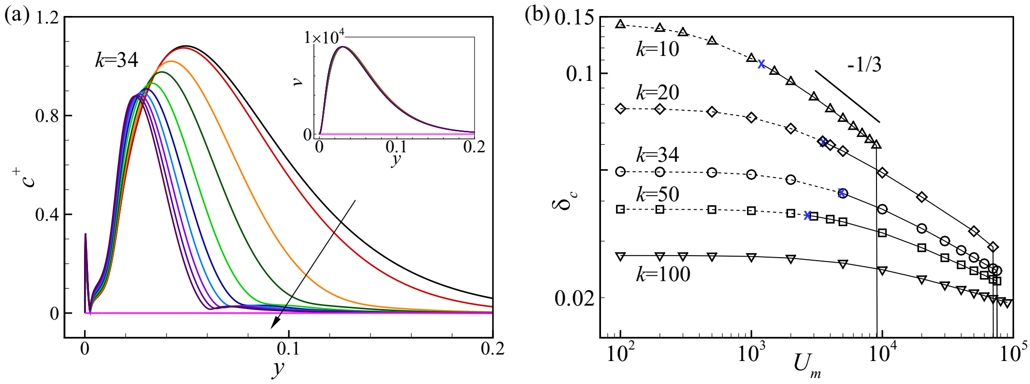

FIG. 15. (a) The magnitude of the perturbed cation concentration distribution in the purely EC instability at different imposed velocities, inset shows the velocity profiles, $\delta = 10^{-4}$, $V = 25$, and $k = 34$. The imposed flow velocity is $U_m = 0$, 10^3, 5×10^3, 10^4, 2×10^4, 3×10^4, 4×10^4, 5×10^4, 6×10^4, 7×10^4, and 8×10^4, respectively. (b) The dependence of the position of the maximum concentration perturbation δ_c on the imposed velocity at different wave numbers. The dashed and solid lines represent the unstable and stable regimes, respectively. The blue X shows the condition of neutral stability.

at large wave numbers or the wave number of the most unstable mode. In Fig. 14(b), the critical voltage V_{cr} for the onset of the EC instability increases with increasing U_m. At the same velocity, the increase of the critical voltage is more prominent when the double layer thickness δ is larger, meaning that suppression of electroconvection by a cross flow is more effective in an electrolyte with low salt concentration. This is because at the same voltage, the wave number of the most unstable mode decreases with increasing δ (see Fig. 10), and the imposed flow is more effective in suppressing the instabilities at small wave numbers. The voltage difference roughly scales as $V_{\mathrm{cr}} - V_{\mathrm{cr},0} \sim (U_m\delta)^{1/2}$, where $V_{\mathrm{cr},0}$ is the critical voltage at $U_m = 0$. The imposed flow suppreses EC instability mode below a wave number k if its strength overcomes the perturbed EC field induced by the second-kind slip velocity, i.e., $U_m \sim k^2V^2$. The scaling $V_{\mathrm{cr}} - V_{\mathrm{cr},0} \sim (U_m\delta)^{1/2}$ suggests that the EC instability is fully suppressed when the imposed flow stabilizes the mode of $k \sim \delta^{-1/2}$. This wave number is lower than $k \sim \delta_s^{-1} \sim (\delta V)^{-2/3}$ corresponding to the space charge layer, suggesting that the interaction between the imposed velocity and the perturbation field plays a role in stabilizing the modes of $\delta^{-1/2} < k < (\delta V)^{-2/3}$.

The mechanism by which the cross flow suppresses EC modes with wave numbers in the range $\delta^{-1/2} < k < \delta^{-2/3}$ can be understood from the eigenfunctions of the perturbed ion concentration in Fig. 15(a). Here, the magnitude of the velocity perturbation is normalized to have the same peak for each case. It is clear that the imposed flow does not influence the EC velocity; instead it reduces the magnitude of the concentration field and more importantly it compresses the concentration perturbation region closer to the space charge layer. The peak of the concentration perturbation decreases from $\delta_c \approx 0.05$ for $U_m = 0$ to $\delta_c \approx 0.025$ at $U_m = 7 \times 10^4$, becoming similar to the space charge layer thickness $\delta_s \approx 0.02$. This effect may cause the stabilization of the modes with $\delta^{-1/2} < k < \delta^{-2/3}$. At $U_m = 8 \times 10^4$, the perturbation completely vanishes near $y = 0$, showing that the imposed flow now directly suppresses the modes with $k \sim \delta^{-2/3}$. In the bulk analysis, this corresponds to the transition from the A branch to P branch for which the solution has negligible electroconvection and a Gaussian distribution of concentration, as discussed in Sec. III.A. Figure 15(b) shows that the imposed velocity decreases δ_c at all wave numbers. For the modes with $k \ll \delta_s^{-1}$, $\delta_c \sim U_m^{-1/3}$ at large U_m. This result, which can be derived by balancing convection of c^+ with its diffusion perpendicular to the wall in a boundary layer analysis of Eq. (35), is consistent with the classical result for a low-Re mass transport [63]. At smaller U_m and high wave numbers, δ_c exhibits a weaker dependence on U_m because other terms, such as diffusion in the tangent

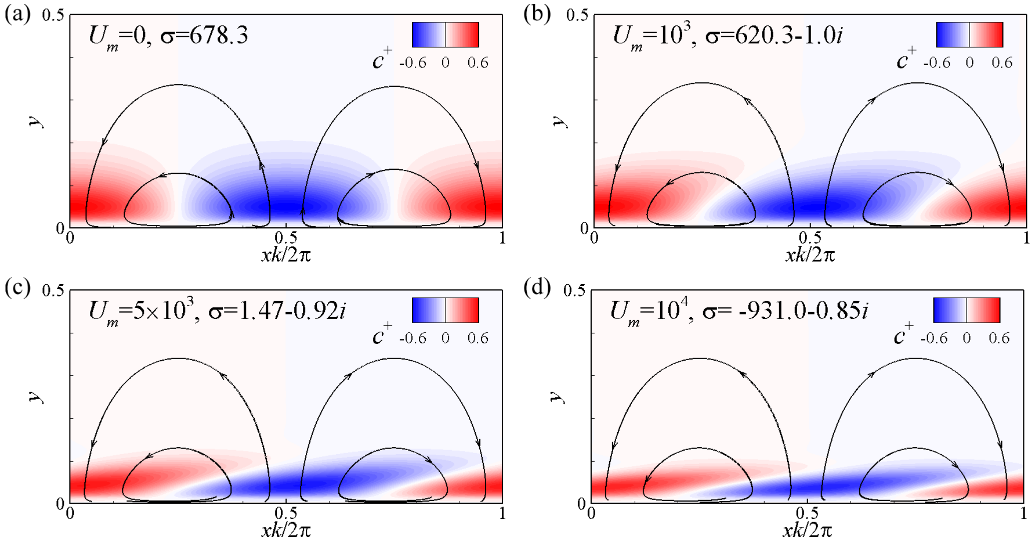

FIG. 16. Cation concentration distribution and the streamlines of the perturbation fluid velocity in the purely EC instability at different imposed velocities, $\delta = 10^{-4}$, $V = 25$, and $k = 34$.

direction and convection by the perturbed velocity, which is most prominent near the surface, become important. To better understand this mechanism, we further plot the two-dimensional (2D) perturbation field in Fig. 16. Here, the plots are normalized such that all the results have the same maximum normal velocity. At $U_m = 0$, both ion concentration and fluid velocity have real eigenfunctions, corresponding to stationary vortices which bring more ions from low- to high-concentration regions and therefore cause the instability when the convective flux is stronger than the stabilizing effect of ion diffusion. The imposed flow has a small influence on the streamlines of the disturbance flow and its main effect is on the concentration field. The shear flow near the wall deforms the ion concentration and generates an inclined shielded region which hinders the ion flux from low- to high-concentration regions. With increasing velocity, the stretching of the perturbed ion concentration field becomes stronger and it eventually stabilizes the perturbation.

Finally, we compare our linear stability analysis with results in the literature. In most previous studies [49–51], electroconvection is always observed because the imposed flow is well below the minimum velocity to fully suppress the instability. The simulations by Urtenov *et al.* [49] and Nikonenko *et al.* [50] are performed at $V = 40$–72, $U_m \approx 1400$–2800, and $\delta = 10^{-5}$–2×10^{-4} showing no signature of stabilization. We estimate that at $V = 40$, $U_m \approx 10^5$ and 10^6 are needed to fully suppress the EC instability for $\delta = 10^{-4}$ and $\delta = 10^{-5}$, respectively, thus being consistent with their results. We also compare the analysis with the simulation results of a developing channel flow of electrolyte by Kwak *et al.* [3]. At $\delta = 1.38 \times 10^{-3}$, $\mathrm{Pe} = 0.35$, $D = 0.67$, and $V = 22$, the linear stability analysis predicts that the EC instability is stabilized at $U_m \approx 207$, which is similar to the simulation result showing that EC vortices are fully suppressed around $U_m = 180$. The difference may be caused by entrance effects in the simulation.

D. Electroconvective/morphological instability

Figure 17(a) shows the growth rate of the perturbation for the EC/Morph instability at two different voltages, $V = 15$ and 25, which are below and above the critical voltage for the onset of electroconvection, respectively. At $V = 15$, the full analysis agrees well with the asymptotic solutions of the bulk problem $\sigma_r \approx 1$ for $k \ll 1$ and $\sigma \approx k$ for $k \gg 1$. The Morph instability is directly caused by the cation flux and therefore is not strongly influenced by the space charge layer.

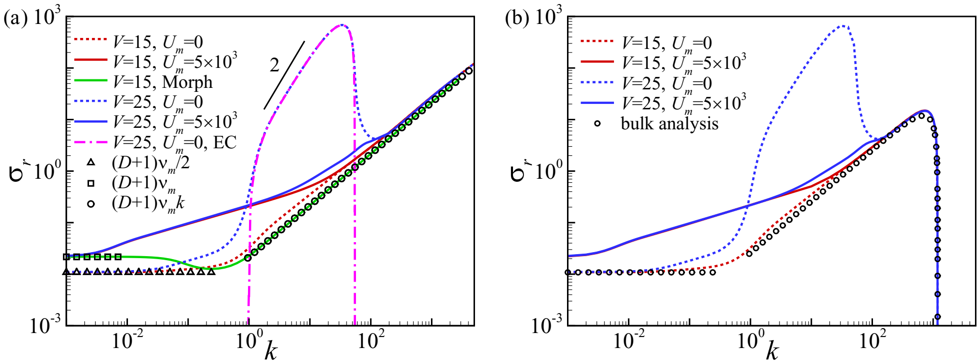

FIG. 17. (a) Maximum growth rate of the EC/Morph instability at $\delta = 10^{-4}$. $V = 15$ and $V = 25$ are below and above the critical voltage for the onset of the EC instability at $U_m = 0$. Symbols show the asymptotic solutions in Eqs. (25), (26), and (31) for the bulk analysis. (b) Maximum growth rate of the instability with surface tension at the electrode/electrolyte interface. The bulk analysis result shows the growth rate for the purely Morph instability at large wave number (39) with $C|_{y=0} = 0.15$.

At $V = 25$, the growth of the ion-depositing surface gains a signature from the EC instability. The growth rate has a region where $\sigma_r \sim k^2$ due to the EC instability. It reaches a local maximum at $k \simeq 30$ and eventually scales as k again as $k \to \infty$. This result is qualitatively different from the bulk analysis in Ref. [41], showing that the full analysis is necessary to correctly predict the EC/Morph instability. With a strong cross flow, the local peak of the growth rate due to the EC instability vanishes.

At sufficiently large wave number, the surface tension of the electrode/electrolyte interface eventually becomes important and stabilizes the surface. To consider the effects of surface tension, we replace the boundary condition for the cation in Eq. (2a) by the electrochemical potential balance at the electrolyte/electrode interface [64],

$$\Phi^{\theta}_{C^+} + (\Phi + \ln C^+)|_{y=h} = \Phi^{\theta}_m + \Phi_m + \gamma K, \tag{37}$$

where $\Phi^{\theta}_{C^+}$ and Φ^{θ}_m are the standard chemical potentials for the cation in the electrolyte and metal electrode, respectively, and Φ_m is the electrostatic potential of the metal electrode. $\gamma = \gamma^* v^*_m/(LRT)$ is the capillary number of the depositing cation. For the lithium metal, the molar volume of the metal atom is $v^*_m = 1.33 \times 10^{-5}$ m^3/mol, the interfacial energy $\gamma^* = 1.716$ J/m^2, and the dimensionless interfacial energy $\gamma = 9.15 \times 10^{-6}$. K is the curvature of the electrode surface, which is positive for a convex projection into the electrolyte. In the base state, Eq. (37) reduces to the condition (2a) for a constant cation concentration. Here, we still assume $C^+|_{y=0} = C_s = 1$. For small perturbations, $K = -d^2h/dx^2$ and the boundary condition at the anode surface in Eq. (36a) becomes

$$(c^+ + C^{+'} h)|_{y=0} = h\gamma k^2 C^+|_{y=0}. \tag{38}$$

The corresponding growth rate is shown in Fig. 17(b). The surface tension stabilizes the perturbation for $k > 10^3$ and the critical wave number scales as $k \sim \gamma^{-1/2}$ [64]. Similarly, for the bulk analysis, we replace the first boundary condition in Eq. (9a) by a chemical potential balance condition for the cation $2(c|_{y=0} + h)/C|_{y=0} - \mu|_{y=0} = h\gamma k^2$. $C|_{y=0}$ is the small but nonzero cation concentration at the edge of the bulk region and here we treat it as a fitting parameter. The growth rate in Eq. (31) becomes

$$\sigma = (D + 1)v_m k(1 - C|_{y=0}\gamma k^2/2), \tag{39}$$

and the mode becomes stable at $k_{\text{cr}} = \sqrt{2/(\gamma C|_{y=0})}$. In Fig. 17(b), the bulk analysis matches the full analysis for large k with a fitting parameter $C|_{y=0} \approx 0.15$. This result shows that the double layer and the space charge layer have significant effects on the Morph instability at sufficiently high wave numbers. However, it is not straightforward to directly compare the bulk and full analysis since the boundaries in the two analyses are different. It is thus important to experimentally determine the ion concentration at the electrode/electrolyte interface to accurately predict the critical wave number at which the interfacial energy becomes important using the bulk analysis. To summarize, although the cross flow cannot eliminate the Morph instability, it does affect the wave number of the most unstable mode by suppressing electroconvection.

This result is qualitatively consistent with previous experiments which observed the change in the morphology of metal electrodeposition resulting from suppression of the EC instability. In the presence of the EC instability, zinc deposition at the microscopic scale displays an orderly alignment of grain flakes (1 μm by 2 μm by 100 nm) with a preferred orientation, which involves two length scales, the small wavelength ($\approx$1 μm) determined by an individual grain and the large wavelength ($\approx 10^2$ μm) set by the groups of arrayed grains with the same orientation. When the EC instability is suppressed by adding agar gel into the electrolyte, the zinc deposition has a morphology of randomly oriented grains which only has the small wavelength [37]. This morphology change at the microscopic scale causes the transition from an ordered dendritic deposition to a dense branch deposition at the macroscopic scale [36,37]. More recently, Wei *et al.* [38] showed that lithium deposition on a planar metal electrode surface transitions from mossy mushroom structures (large wavelength) to needle-like structures (small wavelength) as electroconvection is suppressed by adding high-molecular-weight molecules into the electrolyte. Our results predict that similar effects can be achieved by imposing flow.

V. CONCLUSION

We studied the effects of cross flow on the EC and Morph instabilities in an electrolyte near an ion-selective surface using two methods. In the bulk analysis, we use the electro-osmotic slip velocities as the boundary conditions for the bulk region and derive the asymptotic solutions for small and large wave numbers. In the full analysis, we numerically calculate the base state as well as the perturbed solution using the ultraspherical spectral method. In both studies, the general effect of the cross flow is to attenuate the influences of the electroconvection by suppressing the vortices at small wave numbers near the ion-selective surface. For the purely EC instability, the imposed flow generates a stable central mode below a critical wave number and decreases the growth rate of the unstable wall mode at large wave numbers. The transition between the two modes occurs at the transition wave number $k_t \sim U_m^{1/2} V^{-1}$ at which the imposed velocity equals the second-kind slip velocity. The influence of the imposed flow on the EC instability can be distinguished in three regimes. For $U_m < V^2 \delta^{-1}$, the EC modes with $k < k_t$ and $k > \delta^{-2/3}$ are suppressed by the flow and the space charge layer, respectively, while the modes with $k_t < k < \delta^{-2/3}$ are unstable. For $U_m > V^{2/3} \delta^{-4/3}$, all EC modes are suppressed because the imposed flow overwhelms the EC flow at all wave numbers up to $k \sim \delta^{-2/3}$, above which the modes are suppressed by the space charge layer. Interestingly, in the regime in between, all EC modes are also fully suppressed through a different mechanism. The interaction between the imposed flow and the perturbed concentration field outside the space charge layer stabilizes the modes of $\delta^{-1/2} < k < \delta^{-2/3}$. More specifically, the shear flow creates a sheltering effect by distorting the concentration field and prevents the EC vortex-induced ion flux from low- to high-concentration regions which causes the instability. This effect leads to the $V \sim (U_m \delta)^{1/2}$ scaling for the increase of critical voltage for the onset of EC instability.

In spite of the imposed flow, a metal electrode adjacent to a Newtonian electrolyte is always subject to the Morph instability. Its growth rate scales as $\sigma \approx 1$ for $k \ll 1$ and $\sigma \sim k$ for $k \gg 1$. The onset of the EC instability greatly increases the growth rate of the Morph instability to $\sigma \sim k^2$ and generates a local maximum at a moderate wave number ($k \approx 10$). In this scenario, the ion deposition acquires signatures from both Morph and EC instabilities. For example, zinc deposition has a microscale morphology of an orderly alignment of grain flakes with a preferred orientation. This structure has both small (individual grain) and large (ordered structure) wavelengths [37]. The imposed flow increases the growth rate at small wave number ($k < 10^{-1}$) by increasing the ion concentration gradient near the electrolyte/electrode interface. At large wave number, the flow reduces the growth rate mainly by suppressing the EC instability at $k \approx 10$. The suppression of the EC instability removes the EC signature and changes the morphology of the electrodeposition. This effect is expected to be similar to the results of using gels and polymers to suppress EC flow and change the deposition morphology [36–38].

The comparison between the analytical treatment of the bulk region and the full stability analysis shows that the analytical result must be used with caution. For the purely EC instability, the bulk analysis significantly underestimates the critical voltage and fails to predict the transition from unstable to stable modes with increasing wave number. When the applied voltage is well above the critical voltage for the onset of the EC instability, the transition wave number from the full calculation scales as the inverse of the thickness of the space charge layer $k \sim \delta^{-2/3}$, a result that might be anticipated by applying a simple cutoff to the bulk analysis. When the applied voltage is close to the critical voltage, however, no such relation was found, suggesting a more complicated interaction between the perturbation and the space charge layer which can only be captured by the full analysis. For the EC instability without the flow, the perturbed velocity transports more ions from regions of low concentration to regions of high concentration than predicted by the bulk analysis. Once the flow is strong enough to overcome the stabilizing effects caused by ion diffusion and migration, it generates a positive feedback and causes the EC instability. By studying the transition from unstable to stable modes at various double layer thicknesses and applied voltages, our result shows that the base state becomes stable when the maximum normal velocity $v_{\max} < 0.22k^2V$ for an ion concentration with a unitary peak. The stabilizing effect of the imposed flow is not caused by reducing the perturbation velocity. In fact, the magnitude of the perturbation velocity increases with increasing magnitude of the imposed flow. Instead, the shear flow deforms the perturbed ion concentration field and generates a shielding effect which suppresses the ion flux from low- to high-concentration regions. The bulk analysis qualitatively captures these features but the results are quantitatively different from those obtained with the full analysis. For the purely Morph instability, the bulk analysis predicts accurate results for both small and large wave numbers. However, when the surface tension becomes important, the ion concentration distribution near the ion-selective surface, which must be determined from the full analysis or experimental measurements, significantly affects the prediction of the critical wave number.

ACKNOWLEDGMENTS

This research is supported by Department of Energy Basic Energy Science Grant No. DE-SC0016082.

---

[1] S. J. Kim, S. H. Ko, K. H. Kang, and J. Han, Direct seawater desalination by ion concentration polarization, Nat. Nanotechnol. **5**, 297 (2010).

[2] E. Kjeang, N. Djilali, and D. Sinton, Microfluidic fuel cells: A review, J. Power Sources **186**, 353 (2009).

[3] R. Kwak, V. S. Pham, K. M. Lim, and J. Han, Shear Flow of an Electrically Charged Fluid by Ion Concentration Polarization: Scaling Laws for Electroconvective Vortices, Phys. Rev. Lett. **110**, 114501 (2013).

[4] R. Kwak, V. S. Pham, and J. Han, Sheltering the perturbed vortical layer of electroconvection under shear flow, J. Fluid Mech. **813**, 799 (2017).

[5] M. M. Jakšić, Hydrodynamic effects on the macromorphology of electrodeposited zinc and flow visualization: A flat plate electrode in a channel flow cell, J. Electroanal. Chem. Interfacial Electrochem. **249**, 35 (1988).

[6] M. N. Parekh, C. D. Rahn, and L. A. Archer, Controlling dendrite growth in lithium metal batteries through forced advection, J. Power Sources **452**, 227760 (2020).

[7] M. N. Parekh and C. D. Rahn, Reducing dendrite growth in lithium metal batteries by creeping Poiseuille and Couette flows, J. Electrochem. Soc. **167**, 160525 (2020).

[8] S. M. Rubinstein, G. Manukyan, A. Staicu, I. Rubinstein, B. Zaltzman, R. G. H. Lammertink, F. Mugele, and M. Wessling, Direct Observation of a Nonequilibrium Electro-Osmotic Instability, Phys. Rev. Lett. **101**, 236101 (2008).

[9] J. C. de Valença, R. M. Wagterveld, R. G. H. Lammertink, and P. A. Tsai, Dynamics of microvortices induced by ion concentration polarization, Phys. Rev. E **92**, 031003(R) (2015).

[10] S. J. Kim, Y.-C. Wang, J. H. Lee, H. Jang, and J. Han, Concentration Polarization and Nonlinear Electrokinetic Flow Near a Nanofluidic Channel, Phys. Rev. Lett. **99**, 044501 (2007).

[11] G. Yossifon and H.-C. Chang, Selection of Nonequilibrium Overlimiting Currents: Universal Depletion Layer Formation Dynamics and Vortex Instability, Phys. Rev. Lett. **101**, 254501 (2008).

[12] I. Rubinstein and B. Zaltzman, Electro-osmotically induced convection at a permselective membrane, Phys. Rev. E **62**, 2238 (2000).

[13] I. Rubinstein and B. Zaltzman, Electro-osmotic slip of the second kind and instability in concentration polarization at electrodialysis membranes, Math. Models Methods Appl. Sci. **11**, 263 (2001).

[14] I. Rubinstein, B. Zaltzman, and I. Lerman, Electroconvective instability in concentration polarization and nonequilibrium electro-osmotic slip, Phys. Rev. E **72**, 011505 (2005).

[15] B. Zaltzman and I. Rubinstein, Electro-osmotic slip and electroconvective instability, J. Fluid Mech. **579**, 173 (2007).

[16] E. A. Demekhin, N. V. Nikitin, and V. S. Shelistov, Direct numerical simulation of electrokinetic instability and transition to chaotic motion, Phys. Fluids **25**, 122001 (2013).

[17] E. A. Demekhin, N. V. Nikitin, and V. S. Shelistov, Three-dimensional coherent structures of electrokinetic instability, Phys. Rev. E **90**, 013031 (2014).

[18] C. L. Druzgalski, M. B. Andersen, and A. Mani, Direct numerical simulation of electroconvective instability and hydrodynamic chaos near an ion-selective surface, Phys. Fluids **25**, 110804 (2013).

[19] C. Druzgalski and A. Mani, Statistical analysis of electroconvection near an ion-selective membrane in the highly chaotic regime, Phys. Rev. Fluids **1**, 073601 (2016).

[20] G. Li, L. A. Archer, and D. L. Koch, Electroconvection in a Viscoelastic Electrolyte, Phys. Rev. Lett. **122**, 124501 (2019).

[21] H.-C. Chang, G. Yossifon, and E. A. Demekhin, Nanoscale electrokinetics and microvortices: How microhydrodynamics affects nanofluidic ion flux, Annu. Rev. Fluid Mech. **44**, 401 (2012).

[22] A. Mani and K. M. Wang, Electroconvection near electrochemical interfaces: Experiments, modeling, and computation, Annu. Rev. Fluid Mech. **52**, 509 (2020).

[23] W. W. Mullins and R. F. Sekerka, Stability of a planar interface during solidification of a dilute binary alloy, J. Appl. Phys. **35**, 444 (1964).

[24] V. Fleury, J. N. Chazalviel, and M. Rosso, Coupling of drift, diffusion, and electroconvection, in the vicinity of growing electrodeposits, Phys. Rev. E **48**, 1279 (1993).

[25] J. M. Huth, H. L. Swinney, W. D. McCormick, A. Kuhn, and F. Argoul, Role of convection in thin-layer electrodeposition, Phys. Rev. E **51**, 3444 (1995).

[26] Y. Sawada, A. Dougherty, and J. P. Gollub, Dendritic and Fractal Patterns in Electrolytic Metal Deposits, Phys. Rev. Lett. **56**, 1260 (1986).

[27] D. Grier, E. Ben-Jacob, R. Clarke, and L.-M. Sander, Morphology and Microstructure in Electrochemical Deposition of Zinc, Phys. Rev. Lett. **56**, 1264 (1986).

[28] F. Argoul, A. Arneodo, G. Grasseau, and H. L. Swinney, Self-Similarity of Diffusion-Limited Aggregates and Electrodeposition Clusters, Phys. Rev. Lett. **61**, 2558 (1988).

[29] J.-N. Chazalviel, Electrochemical aspects of the generation of ramified metallic electrodeposits, Phys. Rev. A **42**, 7355 (1990).

[30] V. Fleury, J.-N. Chazalviel, and M. Rosso, Theory and Experimental Evidence of Electroconvection around Electrochemical Deposits, Phys. Rev. Lett. **68**, 2492 (1992).

[31] W. Mu, W. J. P. van Enckevort, N.-b. Ming, and P. Bennema, Formation of a mesh-like electrodeposit induced by electroconvection, Nature (London) **367**, 438 (1994).

[32] F. Maletzki, H.-W. Rösler, and E. Staude, Ion transfer across electrodialysis membranes in the overlimiting current range: Stationary voltage current characteristics and current noise power spectra under different conditions of free convection, J. Membr. Sci. **71**, 105 (1992).

[33] R. Khurana, J. L. Schaefer, L. A. Archer, and G. W. Coates, Suppression of lithium dendrite growth using cross-linked polyethylene/poly (ethylene oxide) electrolytes: A new approach for practical lithium-metal polymer batteries, J. Am. Chem. Soc. **136**, 7395 (2014).

[34] J.-H. Han, M. Wang, P. Bai, F. R. Brushett, and M. Z. Bazant, Dendrite suppression by shock electrodeposition in charged porous media, Sci. Rep. **6**, 28054 (2016).

[35] S. Stalin, M. Tikekar, P. Biswal, G. Li, H. E. N. Johnson, Y. Deng, Q. Zhao, D. Vu, G. W. Coates, and L. A. Archer, Designing polymeric interphases for stable lithium metal deposition, Nano Lett. **20**, 5749 (2020).

[36] M. Wang, N.-b. Ming, and P. Bennema, Pattern formation in noise-reduced electrochemical deposition, Phys. Rev. E **48**, 3825 (1993).

[37] Y. Tu, X. Chao, J. Sang, S. Huang, and X. Zou, Thin-layer electrodeposition of Zn in the agar gel medium, Physica A (Amsterdam, Neth.) **387**, 4007 (2008).

[38] S. Wei, Z. Cheng, P. Nath, M. D. Tikekar, G. Li, and L. A. Archer, Stabilizing electrochemical interfaces in viscoelastic liquid electrolytes, Sci. Adv. **4**, eaao6243 (2018).

[39] D. Zhang, A. J. Warren, G. Li, Z. Cheng, X. Han, Q. Zhao, X. Liu, Y. Deng, and L. A. Archer, Electrodeposition of zinc in aqueous electrolytes containing high molecular weight polymers, Macromolecules **53**, 2694 (2020).

[40] S. Choudhury, G. Li, R. R. Singh, A. Warren, X. Liu, and L. A. Archer, Structure, rheology, and electrokinetics of soft colloidal suspension electrolytes, Langmuir **36**, 9047 (2020).

[41] M. D. Tikekar, G. Li, L. A. Archer, and D. L. Koch, Electroconvection and morphological instabilities in potentiostatic electrodeposition across liquid electrolytes with polymer additives, J. Electrochem. Soc. **165**, A3697 (2018).

[42] E. Karatay, M. B. Andersen, M. Wessling, and A. Mani, Coupling between Buoyancy Forces and Electroconvective Instability Near Ion-Selective Surfaces, Phys. Rev. Lett. **116**, 194501 (2016).

[43] M. B. Andersen, K. M. Wang, J. Schiffbauer, and A. Mani, Confinement effects on electroconvective instability, Electrophoresis **38**, 702 (2017).

[44] A. J. Bard and L. R. Faulkner, *Electrochemical Methods: Fundamentals and Applications*, 2nd ed. (John Wiley & Sons, INC, New York, 2001).

[45] J. Zheng, J. Yin, D. Zhang, G. Li, D. C. Bock, T. Tang, Q. Zhao, X. Liu, A. Warren, Y. Deng *et al.*, Spontaneous and field-induced crystallographic reorientation of metal electrodeposits at battery anodes, Sci. Adv. **6**, eabb1122 (2020).

[46] M. R. H. Hill and G. T. Rogers, Polyethylene glycol in copper electrodeposition onto a rotating disk electrode, J. Electroanal. Chem. Interfacial Electrochem. **86**, 179 (1978).

[47] M. M. Jakšić, Hydrodynamic effects on the macromorphology of electrodeposited zinc and flow visualization: The rotating disk electrode, J. Electroanal. Chem. Interfacial Electrochem. **249**, 63 (1988).

[48] S. V. Pham, H. Kwon, B. Kim, J. K. White, G. Lim, and J. Han, Helical vortex formation in three-dimensional electrochemical systems with ion-selective membranes, Phys. Rev. E **93**, 033114 (2016).

[49] M. K. Urtenov, A. M. Uzdenova, A. V. Kovalenko, V. V. Nikonenko, N. D. Pismenskaya, V. I. Vasil’eva, P. Sistat, and G. Pourcelly, Basic mathematical model of overlimiting transfer enhanced by electroconvection in flow-through electrodialysis membrane cells, J. Membr. Sci. **447**, 190 (2013).

[50] V. V. Nikonenko, V. I. Vasil’eva, E. M. Akberova, A. M. Uzdenova, M. K. Urtenov, A. V. Kovalenko, N. P. Pismenskaya, S. A. Mareev, and G. Pourcelly, Competition between diffusion and electroconvection at an ion-selective surface in intensive current regimes, Adv. Colloid Interface Sci. **235**, 233 (2016).

[51] V. V. Nikonenko, A. V. Kovalenko, M. K. Urtenov, N. D. Pismenskaya, J. Han, P. Sistat, and G. Pourcelly, Desalination at overlimiting currents: State of the art and perspectives, Desalination **342**, 85 (2014).

[52] H. Lin, B. D. Storey, M. H. Oddy, C.-H. Chen, and J. G. Santiago, Instability of electrokinetic microchannel flows with conductivity gradients, Phys. Fluids **16**, 1922 (2004).

[53] C.-H. Chen, H. Lin, S. K. Lele, and J. G. Santiago, Convective and absolute electrokinetic instability with conductivity gradients, J. Fluid Mech. **524**, 263 (2005).

[54] J. D. Posner, C. L. Pérez, and J. G. Santiago, Electric fields yield chaos in microflows, Proc. Natl. Acad. Sci. USA **109**, 14353 (2012).

[55] H. J. White, *Industrial Electrostatic Precipitation* (Addison-Wesley, Reading, MA, 1963).

[56] M. Zhang, F. Martinelli, J. Wu, P. J. Schmid, and M. Quadrio, Modal and non-modal stability analysis of electrohydrodynamic flow with and without cross-flow, J. Fluid Mech. **770**, 319 (2015).

[57] M. Zhang, Weakly nonlinear stability analysis of subcritical electrohydrodynamic flow subject to strong unipolar injection, J. Fluid Mech. **792**, 328 (2016).

[58] F. Li, B.-F. Wang, Z.-H. Wan, J. Wu, and M. Zhang, Absolute and convective instabilities in electrohydrodynamic flow subjected to a Poiseuille flow: A linear analysis, J. Fluid Mech. **862**, 816 (2019).

[59] S. Olver and A. Townsend, A fast and well-conditioned spectral method, SIAM Rev. **55**, 462 (2013).

[60] J. A. Weideman and S. C. Reddy, A MATLAB differentiation matrix suite, ACM Trans. Math. Softw. **26**, 465 (2000).

[61] P. J. Schmid and D. S. Henningson, *Stability and Transition in Shear Flows*, Applied Mathematical Sciences Vol. 142 (Springer Science & Business Media, Berlin, 2012).

[62] E. A. Demekhin, V. S. Shelistov, and S. V. Polyanskikh, Linear and nonlinear evolution and diffusion layer selection in electrokinetic instability, Phys. Rev. E **84**, 036318 (2011).

[63] L. G. Leal, *Advanced Transport Phenomena: Fluid Mechanics and Convective Transport Processes*, Cambridge Series in Chemical Engineering Vol. 7 (Cambridge University Press, Cambridge, UK, 2007).

[64] M. D. Tikekar, L. A. Archer, and D. L. Koch, Stability analysis of electrodeposition across a structured electrolyte with immobilized anions, J. Electrochem. Soc. **161**, A847 (2014).